Ore Geology Reviews 65 (2015) 853–871

Contents lists available at ScienceDirect

Ore Geology Reviews

journal homepage: www.elsevier.com/locate/oregeorev

In-situ LA-ICP-MS trace elemental analyses of magnetite: Fe–Ti–(V) oxide-bearing mafic–ultramafic layered intrusions of the Emeishan Large Igneous Province, SW China

Ping-Ping Liu [a], Mei-Fu Zhou [a,*], Wei Terry Chen [a], Jian-Feng Gao [b], Xiao-Wen Huang [c]

[a] Department of Earth Sciences, University of Hong Kong, Pokfulam Road, Hong Kong, China
[b] State Key Laboratory for Mineral Deposits Research, Nanjing University, Nanjing 210093, China
[c] State Key Laboratory of Ore Deposit Geochemistry, Institute of Geochemistry, Chinese Academy of Sciences, Guiyang 550002, China

ARTICLE INFO

Article history:
Received 24 April 2014
Received in revised form 29 August 2014
Accepted 1 September 2014
Available online 7 September 2014

Keywords:
LA-ICP-MS
Magnetite
Oxygen fugacity
QUILF
ELIP
SW China

ABSTRACT

The Taihe, Baima, Hongge, Panzhihua and Anyi intrusions of the Emeishan Large Igneous Province (ELIP), SW China, contain large magmatic Fe–Ti–(V) oxide ore deposits. Magnetites from these intrusions have extensive trellis or sandwich exsolution lamellae of ilmenite and spinel. Regular electron microprobe analyses are insufficient to obtain the primary compositions of such magnetites. Instead, laser ablation ICP-MS uses large spot sizes (~40 μm) and can produce reliable data for magnetites with exsolution lamellae. Although magnetites from these deposits have variable trace element contents, they have similar multi-element variation patterns. Primary controls of trace element variations of magnetite in these deposits include crystallography in terms of the affinity of the ionic radius and the overall charge balance, oxygen fugacity, magma composition and coexisting minerals. Early deposition of chromite or Cr-magnetite can greatly deplete magmas in Cr and thus Cr-poor magnetite crystallized from such magmas. Co-crystallizing minerals, olivine, pyroxenes, plagioclase and apatite, have little influence on trace element contents of magnetite because elements compatible in magnetite are incompatible in these silicate and phosphate minerals. Low contents and bi-modal distribution of the highly compatible trace elements such as V and Cr in magnetite from Fe–Ti oxide ores of the ELIP suggest that magnetite may not form from fractional crystallization, but from relatively homogeneous Fe-rich melts. QUILF equilibrium modeling further indicates that the parental magmas of the Panzhihua and Baima intrusions had high oxygen fugacities and thus crystallized massive and/or net-textured Fe–Ti oxide ores at the bottom of the intrusive bodies. Magnetite of the Taihe, Hongge and Anyi intrusions, on the other hand, crystallized under relatively low oxygen fugacities and, therefore, formed net-textured and/or disseminated Fe–Ti oxides after a lengthy period of silicate fractionation. Plots of Ge vs. Ga + Co can be used as a discrimination diagram to differentiate magnetite of Fe–Ti–(V) oxide-bearing layered intrusions in the ELIP from that of massif anorthosites and magmatic Cu–Ni sulfide deposits. Variable amounts of trace elements of magmatic magnetites from Fe–Ti–(P) oxide ores of the Damiao anorthosite massif (North China) and from Cu–Ni sulfide deposits of Sudbury (Canada) and Huangshandong (northwest China) demonstrate the primary control of magma compositions on major and trace element contents of magnetite.

1. Introduction

Magnetite occurs widely in igneous, metamorphic and sedimentary rocks. It can be concentrated to form hydrothermal magnetite deposits (e.g. Bookstrom, 1995; Groves et al., 2010; Nadoll et al., 2012), banded iron formations (BIFs) (Chung et al., 2015; Dymek and Klein, 1988; Klein, 2005) and magmatic Fe–Ti–(V) oxide deposits (Philpotts, 1967; Wager and Brown, 1968). In addition to Fe, magmatic magnetite contains considerable amounts of Ti and V (Klemm et al., 1985; Lister, 1966; Zhou et al., 2005). Magnetite can form continuous solid solutions with ulvospinel, called titanomagnetite. The principle of the transition from Fe oxide to the Ti-containing phase is to replace two Fe^{III} by one Fe^{II} and one Ti^{IV}, with the increase in unit cell size (Cornell and Schwertmann, 2003; Wechsler et al., 1984). The likelihood of substitution depends on many parameters including the similarity of the ionic radii and the valence of the cations, oxygen fugacities, magma/fluid composition, and temperature (Buddington and Lindsley, 1964; Frost and Lindsley, 1991; Goldschmidt, 1937; Lindsley, 1991; Toplis and Carroll, 1995). Magnetite compositions, conversely, can also reflect the physicochemical conditions under which it was formed. Elements commonly incorporated in the magnetite structure include Mg, Al, Sc, Ti, V, Cr, Mn, Co, Ni, Zn, Ga, Ge, Y, Hf, Nb, Mo, Ta and Zr.

* Corresponding author. Tel.: +86 852 28578251; fax: +86 852 25176912.
E-mail address: mfzhou@hku.hk (M.-F. Zhou).

http://dx.doi.org/10.1016/j.oregeorev.2014.09.002
0169-1368/

Chemical compositions of magnetite corresponding to a wide variety of deposit types have been the focus of many studies during the past few decades. Most of the previous studies employed electron microprobe (EMP), which measures a limited number of trace elements such as Mg, Al, Ca, Ti, V, Cr and Mn with a relatively high detection limit of ~0.01 wt.% and a minute beam diameter of <10 μm (e.g. Dupuis and Beaudoin, 2011). Recent development of laser ablation inductively coupled plasma mass spectrometry (LA-ICP-MS) allows in-situ measurement of a large number of trace elements with relatively low detection limit of ~1 ppm (Liu et al., 2008; Nadoll and Koenig, 2011). Magmatic magnetite commonly develops oxy-exsolution of ilmenite and spinel lamellae (Kolker, 1982; Pang et al., 2008b; von Gruenewaldt et al., 1985). The large spot size of laser makes it possible to obtain an average composition of magnetite before oxy-exsolution occurs. Studies of in-situ LA-ICP-MS have embarked on the investigations of hydrothermal magnetite (Huang et al., 2013, 2015; Nadoll et al., 2012) and magnetite in Cu–Ni sulfide deposits (Dare et al., 2012; Gao et al., 2013). Dupuis and Beaudoin (2011) suggested that plots of Ni + Cr vs. Si + Mg, Al/(Zn + Ca) vs. Cu/(Si + Ca), Ni/(Cr + Mn) vs. Ti + V and Ca + Al + Mn vs. Ti + V can be used to discriminate Ni–Cu–(PGE), volcanogenic massive sulfide, iron-oxide–copper–gold, Kiruna apatite–magnetite, banded iron formations, porphyry Cu, Fe–Cu skarn and Fe–Ti–(V) oxide deposits. However, LA-ICP-MS analyses of hydrothermal magnetite by Nadoll et al. (2014) showed that magnetite from porphyry and BIF deposits plot outside the fields suggested by Dupuis and Beaudoin (2011), and they propose

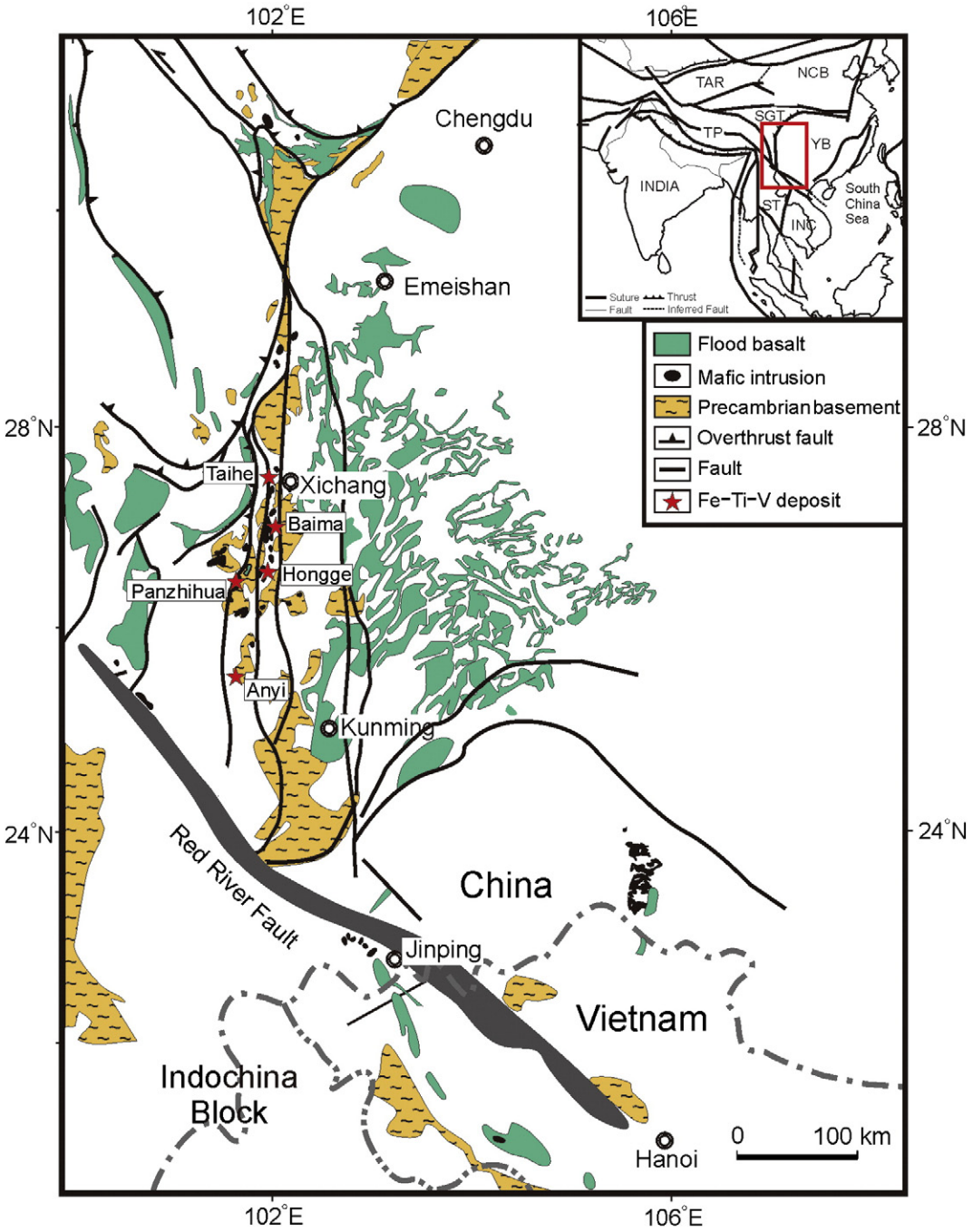

Fig. 1. A simplified geological map of SW China and northern Vietnam (modified after Wang et al., 2007) showing the distribution of the Emeishan basalts, mafic intrusions and associated Fe–Ti–(V) and Ni–Cu–(PGE) deposits within the Emeishan Large Igneous Province (ELIP). Major blocks shown in the inset are: TAR, Tarim; NCB, North China Block; SGT, Songpan–Ganze Terrane; TP, Tibetan Plateau; YB, Yangtze Block; ST, Simao Terrane; INC, Indochina Block.

a combination of Ni/(Cr + Mn) vs. Ti + V, Al + Mn vs. Ti + V, Ti/V and Sn/Ga discriminant diagrams and upper threshold concentrations to fingerprint magnetite from different hydrothermal deposits. Magmatic magnetite from Fe–Ti oxide ores hosted in mafic–ultramafic intrusions, on the other hand, has not been analyzed by LA-ICP-MS.

This paper reports new LA-ICP-MS data of magmatic magnetite from Fe–Ti oxide ores of the Panzhihua, Baima, Hongge, Taihe and Anyi mafic–ultramafic layered intrusions of the ELIP, SW China. Previous studies have demonstrated that these intrusions and high-Ti basalts were probably originated from the same magma in late Permian (Xu et al., 2003; Zhou et al., 2002a, 2008) and experienced various degrees of assimilation and fractional crystallization (AFC) during emplacement. Early crystallization of magnetite in these intrusions is ascribed to high oxygen fugacity conditions (Ganino et al., 2008) or water contents (Howarth et al., 2013). In this paper, we use trace elements of magnetite from these mafic–ultramafic intrusions to investigate the controls on trace element variations of magnetite, and the oxygen fugacity conditions between different intrusions and further discuss the possible significance of magnetite for provenance studies.

2. Geological background

2.1. Regional geology

Southwest China consists of the eastern part of the Tibetan Plateau and the western part of the Yangtze Block (Fig. 1). They are separated by the Songpan–Ganze terrane, which contains southeast–northwest-trending, Late Triassic–Early Jurassic thrust belts filled with >10 km thick sequence of Late Triassic deep marine sediments (Burchfiel et al., 1995). The Cenozoic Tibetan Plateau is a complex terrane formed by accretion of several microcontinents, flysch complexes and island arcs (Yin and Harrison, 2000). The Yangtze Block has a widespread Archean to Mesoproterozoic meta-sedimentary basement, overlain by a middle sequence of Devonian to Triassic strata of marine sedimentary rocks and an upper sequence of Jurassic to Cenozoic strata of mostly terrestrial basin deposits. A Neoproterozoic assemblage of mafic–ultramafic intrusions (780–820 Ma), granite and metamorphic complexes (760–865 Ma) has been identified along the western and northern margins of the Yangtze Block (Zhou et al., 2002b,c). A series of Cenozoic thrust and strike-slip faults dominate in the western margin of the Yangtze Block.

2.2. Emeishan Large Igneous Province

The ELIP, formed in the late Permian (~260 Ma), covers an area of 5×10^5 km^2 from Songpan–Ganzi terrane in SW China in the north to northwestern Vietnam in the south (Chung and Jahn, 1995; Song et al., 2001). It consists of flood basalts, mafic–ultramafic intrusions and syenitic–granitic intrusions. The thickness of the Emeishan volcanic succession ranges from several hundred meters in the east to ~5 km in the west. This large variation probably results from post-eruption tectonic activity leading to strong deformation, uplift and erosion in the Mesozoic and Cenozoic age (Ali et al., 2004). The Emeishan volcanic sequence is composed of picrites, tholeiitic basalts, basaltic andesites and rhyolites (Chung and Jahn, 1995; Xiao et al., 2003). The intrusions of the ELIP are volumetrically small compared to the volcanic rocks, but they are economically important because of the occurrence of Cu–Ni–(PGE) sulfide deposits and Fe–Ti–(V) oxide deposits (Fig. 1). Both volcanic and intrusive rocks are considered to have formed by plume-derived magmas mixed with lithospheric mantle within a short period of 1–2 Ma (Ali et al., 2005; Shellnutt, 2014). The western part of the ELIP has been strongly deformed, uplifted and eroded, leading to the exposure of large intrusions with several kilometers in depth. The Fe–Ti–(V) oxide-bearing mafic–ultramafic layered intrusions are mainly distributed in the Panxi (Panzhihua–Xichang) region of the central ELIP. Several Fe–Ti–(V) oxide ore deposits such as Taihe, Baima, Hongge, Panzhihua and Anyi occur along a north–south-trending linear fault belt (Fig. 1). Regional exploration shows that total Fe–Ti–V ores of the ELIP in the Panxi region are >10 billion tons. The largest deposits include Panzhihua, Hongge, Baima and Taihe, with average grades of 25–55 wt.% Fe, 4–13 wt.% Ti and 0.10–0.45 wt.% V (Ma et al., 2003).

2.3. Geology of the Fe–Ti–(V) oxide-bearing intrusions in the ELIP

The Fe–Ti–(V) oxide-bearing mafic–ultramafic intrusions are spatially and temporally associated with syenitic and granitic intrusions. The large Taihe, Baima, Hongge, Panzhihua and Anyi Fe–Ti–(V) oxide ore deposits have been mined for several to tens of years.

2.3.1. Taihe intrusion

The Taihe mafic intrusion is ~3 km long and 2 km wide, with an approximate thickness of 1.2 km. It extends more than 3 km southeast, dips 50 to 60° SE and surrounded by contemporaneous (~261 ± 2 Ma, Xu et al., 2004) but slightly younger syenite (She et al., 2014; Shellnutt et al., 2011). The mafic rocks are either emplaced by or in fault contact with the syenite. From the base upwards, the intrusion is divided into the lower, middle and upper zones (She et al., 2014). The ~200 m thick lower zone consists of coarse-grained and isotropic (olivine) gabbro, clinopyroxenite, and massive ore. Both the middle and upper zones are characterized by significant amount of apatite of up to 12 vol.%. The ~500 m thick middle zone is dominated by disseminated ore, (olivine) clinopyroxenite and (apatite) gabbro. The upper zone is mainly composed of gabbro with 4 to 10 vol.% apatite. Fe–Ti oxide ores are mainly hosted in the lower zone and the lower part of the middle zone (Fig. 2).

2.3.2. Baima intrusion

The Baima mafic intrusion is ~20 km long and 1 to 4 km wide with an exposure of ~25 km^2. It strikes N–S in general and dips 15–70° W (Liu et al., 2014b). Similar to the Taihe intrusion, the Baima intrusion

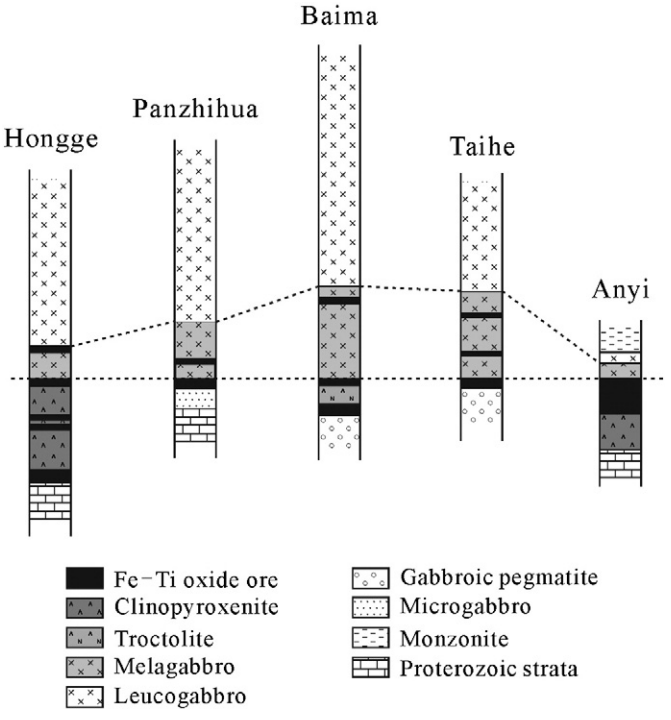

Fig. 2. Petrographic columns of the Fe–Ti oxide ore-bearing Hongge, Panzhihua, Baima, Taihe and Anyi intrusions in the center of the ELIP, showing the position of the Fe–Ti oxide ore layers and the sequence of the host rocks.
Modified after Song et al. (2013).

is also surrounded by a large syenitic pluton with a zircon U–Pb age of ~260 Ma (Shellnutt and Zhou, 2007, 2008; Shellnutt et al., 2012). Both the mafic intrusion and the syenitic pluton intruded the Precambrian Huili group, which has been metamorphosed to marble, schist and migmatitic granite, and carbonate of the Sinian Dengying Formation, which has been metamorphosed to marble along the contact of the intrusion. The Baima mafic intrusion is tectonically dismembered by several NE–SW-trending faults and intruded by abundant syenitic, granitic and dioritic dykes (Liu et al., 2014b; Shellnutt et al., 2009; Zhang et al., 2012; Zhou et al., 2013). It is divided, from base upwards, into the lower and upper zones. Main oxide orebodies are hosted in the lower zone (Fig. 2). Besides, the lower zone also contains interlayered Fe–Ti oxide-bearing troctolite and olivine clinopyroxenite of 150 to 300 m in thickness. The upper zone is mainly composed of 1000 to 1500 m thick olivine gabbro and gabbro.

2.3.3. Hongge intrusion

The Hongge intrusion is approximately 16 km long and 3 to 6 km wide with an exposed area of ~60 km^2 (Panxi Geological Team, 1987). It dips to the east and northeast with a small angle and varies from 580 m to 2700 m in thickness. The footwall rocks are low- to medium-grade metamorphosed, sedimentary–volcanic rocks of the Paleoproterozoic Hekou Formation. The hanging wall is composed of amphibolite and greenschist of the Hekou Formation, dolomite and dolomitic limestone of the Sinian Dengying Formation and the Emeishan flood basalts. A series of NS-, NE- and NW-trending faults crosscut the intrusion and disrupt the continuity of the igneous layering. The Hongge intrusion is composed of the lower, middle and upper zones (Bai et al., 2012; Wang and Zhou, 2013; Zhong et al., 2002). It contains ultramafic rocks in the lower and middle zones (Fig. 2). The 24 to 690 m thick lower zone is composed mostly of olivine clinopyroxenite with thin layers of wehrlite and dunite at the lower part. The 28 to 400-m thick middle zone contains abundant interlayered clinopyroxenites, massive Fe–Ti oxide ores and olivine clinopyroxenites. The 527 to 1346 m thick upper zone consists of fine- to medium-grained gabbro with 2 to 5% apatite.

2.3.4. Panzhihua intrusion

The Panzhihua intrusion is a 19 km long and 2 to 3 km thick gabbroic sill that strikes NE–SW. The sill is cut and displaced by a series of NW-trending faults. It dips 40 to 60° NW and emplaced into dolomitic limestone of the Sinian Dengying Formation. The hanging wall to the west of the intrusion is contemporaneous syenite and Triassic terrestrial clastic rocks. The Panzhihua intrusion is stratigraphically divided into four zones from the base upwards: marginal, lower, middle and upper

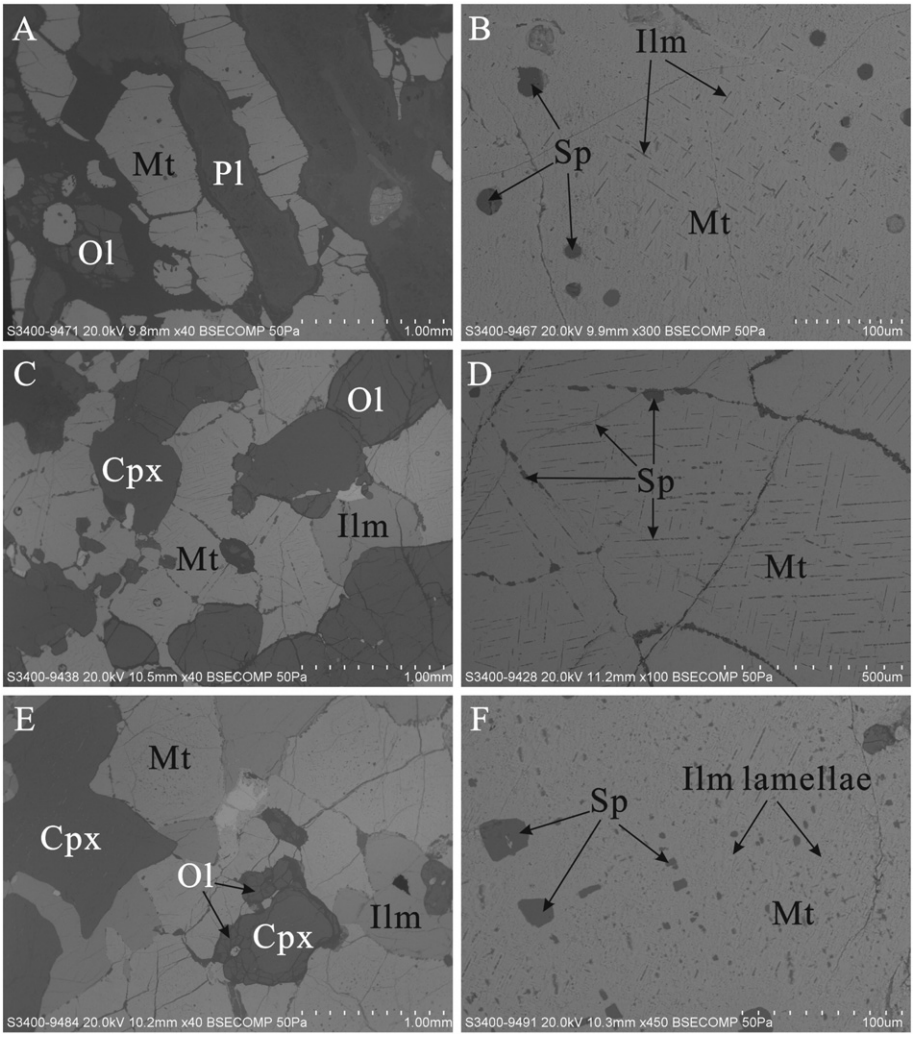

Fig. 3. Scanning electron microscope (SEM) images of Fe–Ti oxide ores in the Panxi region. A) Disseminated Fe–Ti oxide ore from the Taihe deposit showing granular olivine (Ol), plagioclase (Pl) laths and interstitial magnetite (Mt). B) Internal textures of magnetite from the Taihe Fe–Ti oxide ore showing the exsolution of ilmenite (Ilm) lamellae and granular spinel (Sp). C) Net-textured Fe–Ti oxide ore composed of cumulus olivine, clinopyroxene (Cpx) and interstitial magnetite and ilmenite from the Baima intrusion. D) Internal textures of magnetite from the Baima Fe–Ti oxide ore showing the exsolution of spinel lamellae and granular spinel along the magnetite grain boundaries. E) Net-textured Fe–Ti oxide ore consists of cumulus clinopyroxene and interstitial magnetite and ilmenite from the Panzhihua intrusion. Olivine occurs as rim around clinopyroxene. F) Internal textures of magnetite from the Panzhihua Fe–Ti oxide ore showing exsolution lamellae of ilmenite and granular spinel.

zones (Pang et al., 2008a,b; Zhou et al., 2005). The marginal zone consists of fine-grained gabbro and is interpreted to be the chilled base of the intrusion (Pang et al., 2008a). The lower zone is composed dominantly of massive Fe–Ti oxide orebodies with several layers of gabbro. The middle and upper zones are dominated by isotropic gabbro with minor Fe–Ti oxide ore layers in the middle zone (Fig. 2).

2.3.5. Anyi intrusion

The Anyi intrusion is located in the Yuanmou area, about 130 km south of the Panzhihua intrusion. It is ~1.2 km long and 300 to 620 m wide, which extends northeast, with an exposed area of ~0.65 km^2. It intrudes schist and marble of the ~1.0 Ga Julin Group to the north and is unconformably overlain by Cretaceous conglomerate and mudstone to the south (Yu et al., 2014; Zhou et al., 2013). The Anyi intrusion has a zircon SHRIMP U–Pb age of 247 ± 3 Ma, which was interpreted to result from postdated magmatism related to the Emeishan mantle plume (Yu et al., 2014). However, the longevity of the Emeishan mantle plume is preferentially accepted to have a short duration within 1 to 2 Ma (He et al., 2003; Thompson et al., 2001). In addition, the previously reported felsic plutons and dykes with ages of ~252 Ma and ~242 Ma, respectively, in the ELIP analyzed by SHRIMP zircon U–Pb dating (Shellnutt et al., 2008) have been revised to ~260 Ma analyzed by zircon CA-TIMS U–Pb dating (Shellnutt et al., 2012). Therefore, it is possible that the Anyi intrusion might have formed at ~260 Ma, comparable with other mafic–ultramafic intrusions such as Panzhihua and Baima in the ELIP.

The Anyi intrusion has a felsic portion of monzonite and syenite and a mafic–ultramafic portion of Fe–Ti oxide-bearing clinopyroxenite and gabbro (Fig. 2). The mafic–ultramafic body can be divided into the lower and upper zones (Zhou et al., 2013). The lower zone consists of clinopyroxenite and disseminated Fe–Ti oxide ore and the upper zone is made up of gabbro, which grades into monzonite upwards.

3. Petrography of Fe–Ti oxide ores

Oxide ores in the ELIP mainly occur as conformable layers or lenses at the lower or middle part of the layered sequence, resulting in alternating oxide-rich and oxide-poor layers (Bai et al., 2012; Liu et al., 2014b; Pang et al., 2008a, 2009; Wang and Zhou, 2013; Zhang et al., 2012; Zhou et al., 2005, 2013). There are three types of oxide ores in these deposits: massive ore (>85 vol.% Fe–Ti oxides), net-textured ore (35–60 vol.% Fe–Ti oxides) and disseminated ore (15 to 35 vol.% Fe–Ti oxides). The Panzhihua deposit has massive Fe–Ti oxide ores with less than 15 vol.% olivine, plagioclase and clinopyroxene in the lower zone (Fig. 2). Disseminated oxide ores in the middle zone of this deposit contain 15 to 35 vol.% Fe–Ti oxides hosted in coarse-grained gabbro. Net-textured oxide ores are typical in the Hongge and Baima deposits, and are mainly present in the middle zone of the Hongge intrusion and lower zone of the Baima intrusion (Fig. 2). Disseminated oxide ores occur at the base of the lower and middle zones in the Hongge intrusion and at the top of the lower zone in the Baima intrusion. The Taihe intrusion contains massive oxide ores at the top of the lower zone and disseminated oxide ores throughout the middle zone. Oxide ores of the Anyi deposit are mostly disseminated with 15 to 25 vol.% magnetite and ilmenite at the lower part of the intrusion.

Fe–Ti oxide ores of the deposits in the Panxi region are composed of magnetite, ilmenite, olivine, clinopyroxene and plagioclase (Figs. 3 and 4). Magnetite in these ores is polygonal, 0.5–1 mm in diameter and contains relatively crowded trellis ilmenite lamellae, and spinel microintergrowths of small blebs and discontinuous lamellae. Ilmenite also occurs as anhedral, clean and homogeneous crystal with a diameter of 0.3–1 mm. Magnetite and ilmenite occur either as isolated grains in disseminated ores, as interconnected network interstitial to olivine, clinopyroxene and plagioclase in net-textures ores, or as cumulus piles in massive oxide ores.

4. Analytical methods

4.1. Electron microprobe

A JEOL JXA-8100 EMP was used to acquire Fe–Ti oxide mineral composition at the Key Laboratory of Isotope Geochronology and Geochemistry, Guangzhou Institute of Geochemistry, Chinese Academy of

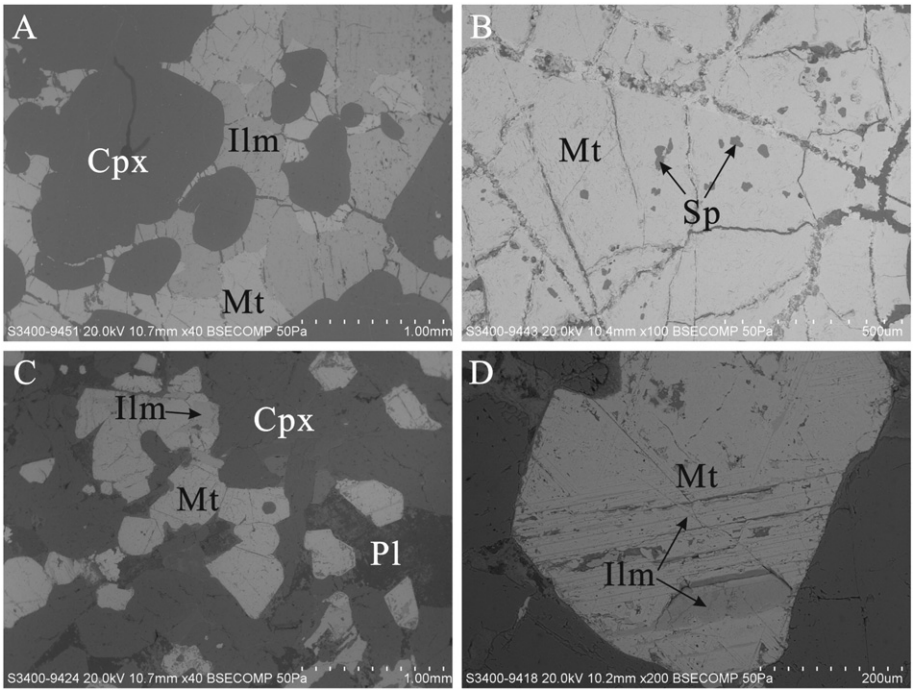

Fig. 4. Scanning electron microscope (SEM) images of Fe–Ti oxide ores in the Panxi region. A) Net-textured Fe–Ti oxide ore from the Hongge intrusion showing granular clinopyroxene crystals and interstitial magnetite and ilmenite. B) Internal textures of magnetite showing granular exsolution of spinel from the Hongge intrusion. C) Disseminated Fe–Ti oxide ore from the Anyi intrusion showing cumulus clinopyroxene, polygonal magnetite grains and interstitial plagioclase. D) Internal textures of magnetite from the Anyi Fe–Ti oxide ore showing exsolution lamellae of ilmenite. Abbreviations are the same as those in Fig. 3.

Sciences. The analyses were carried out under a voltage of 15 kV and a beam current of 20 nA focused to a spot of ~1 μm. Peak and background counting times for major elements were 20 and 10 s, respectively, whereas those for trace elements were 40 and 20 s, respectively. The standards used for oxide analyses were spinel for Mg and Al, ilmenite for Ti, vanadium metal for V, chromite for Cr and Fe, and manganese oxide for Mn. Vanadium concentrations were corrected by analyzing V-free and Ti-bearing standards of rutile and native Ti because of the overlap between Ti Kβ and V Kα peaks (Carmichael, 1966). The precisions of major and trace elements were better than 2% and 5%, respectively. Matrix corrections were performed by the ZAF procedures (Jurek and Hulínský, 1980).

4.2. LA-ICP-MS

To obtain an average composition of titanomagnetite that contains ilmenite exsolution lamellae, a Coherent GeoLasPro 193-nm Laser Ablation system coupled with an Agilent 7700× ICP-MS was used at the State Key Lab of Ore Deposit Geochemistry, Institute of Geochemistry, Chinese Academy of Sciences. USGS standard reference materials, BHVO-2G, BCR-2G, BIR-1G, GSE-1G and NIST610, were used as external standards and ^{57}Fe as internal standard to calibrate element contents (Huang et al., 2013; Liu et al., 2008). Each analysis includes 20 s for measuring the gas blank and 40 s for data acquisition using spot size of 40 μm at 6 Hz with energy of ~100 mJ per pulse. Quality control of time-dependent drift of sensitivity and mass discrimination was monitored by GSE-1G repeated after every eight analyses. The off-line data processing was performed using the program of ICPMSDataCal (Liu et al., 2008).

5. Results

5.1. Compositions of magnetite and ilmenite

Large variations of Al_2O_3, TiO_2 and MgO contents of magnetite obtained by EMP indicate significant variation due to exsolution of ilmenite and spinel (Fig. 5, Appendix A). Magnetite compositions obtained by LA-ICP-MS, however, have smaller variations than those acquired by EMP techniques. They are mostly plotted in the center of the EMP compositional field, representing average magnetite compositions by ablating both magnetite and its exsolution products. Thus, the LA-ICP-MS results of magnetite may represent the original compositions of magnetite.

Multi-element variation diagrams provide an overview of the concentration of a wide range of elements within magnetite. In order to compare various trace element contents in magnetite, lithophile elements of Zr, Hf, Al, W, Sc, Ta, Nb, Ga, Mn, Mg, Ti, V and Cr, normalized to Emeishan high-Ti basalts, are plotted in the order of increasing compatibility (see Dare et al., 2012). It is shown that half of the lithophile elements analyzed including Zr, Hf, Al, Sc, Ta, Nb and Mg in magnetite have concentrations lower than the high-Ti basalts (Fig. 6). Magnetite has slightly higher Ga, Mn, Ti and V contents (less than 10 times), which are relatively compatible, than the high-Ti basalts. Magnetite from the Taihe, Panzhihua, Hongge and Baima deposits has roughly similar distribution curves except that some magnetite grains in the Hongge deposit have extremely high Cr compared with others (Fig. 6). Magnetite from the Anyi deposit, on the other hand, has the most enriched Ta and Nb and the most depleted Mg and Cr contents. Variations of trace element content in magnetite from each deposit can be up to 5–6 orders of magnitude, from <0.01 ppm to more than 1000 ppm in the Panzhihua, Baima, Taihe and Anyi intrusions or even over 10,000 ppm in the Hongge intrusion (Table 1).

In binary plots of Al vs. Mg, V vs. TiO_2, Ga vs. Al, Mn vs. Mg, V vs. Cr, Ni vs. Co, Zn vs. Sn and Hf vs. Zr, plot of V vs. TiO_2 shows a negative correlation whereas there are positive correlations in plots of Al vs. Ga and Hf vs. Zr (Figs. 7 and 8). There are slight differences in trace element

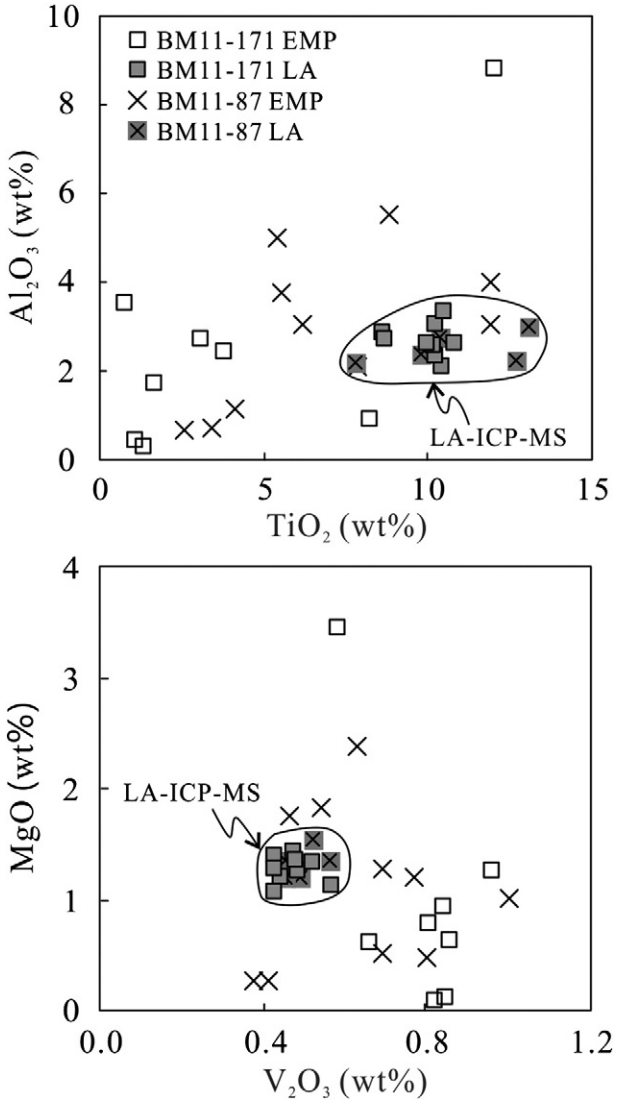

Fig. 5. Al_2O_3 vs. TiO_2 (wt.%) and MgO vs. V_2O_3 (wt.%) diagrams of magnetite from samples BM11-171 and BM11-87 of the Baima Fe–Ti oxide ores analyzed by EMP and LA-ICP-MS.

contents of magnetite from different deposits. For example, magnetite from the Baima deposit has the highest V (4800 to 6300 ppm) but the lowest TiO_2 (5–13 wt.%) contents, whereas magnetite from the Taihe deposit has the lowest V (3500 to 4300 ppm) but the highest TiO_2 (13–19 wt.%) contents. Magnetite from the Panzhihua, Hongge and Anyi deposits has large variations of V and TiO_2 from 3500 to 4700 ppm and 5 to 19 wt.%, respectively, overlapping the field of that of the Baima and Taihe deposits. Magnetite from the Anyi deposit contains the lowest Mg (100 to 800 ppm) and Cr (1 to 10 ppm), and the highest Mn (3400 to 5200 ppm), Sn (3 to 7 ppm), Zn (200 to 5600 ppm), Hf (1 to 3 ppm) and Zr (30 to 120 ppm). Magnetite from the other deposits has more variable Mg, Al, Mn and Cr contents. Magnetite of the Hongge deposit has the highest Cr content of up to 16,000 ppm (Figs. 7 and 8, Table 1), consistent with the presence of Cr-rich magnetite in oxide ores at the bottom of the lower and middle zones reported by Wang and Zhou (2013). Magnetite in the Panzhihua, Taihe and Baima intrusions has relatively low Cr contents ranging from 10 to 600 ppm.

Unlike magnetite, ilmenite composition obtained by electron microprobe is homogeneous. Ilmenite of oxide ores from the Anyi deposit has the lowest MgO (0.05–0.08 wt.%) and highest MnO (1.42–1.64 wt.%) and FeO (46.0–47.6 wt.%) contents, whereas ilmenite of oxide ores

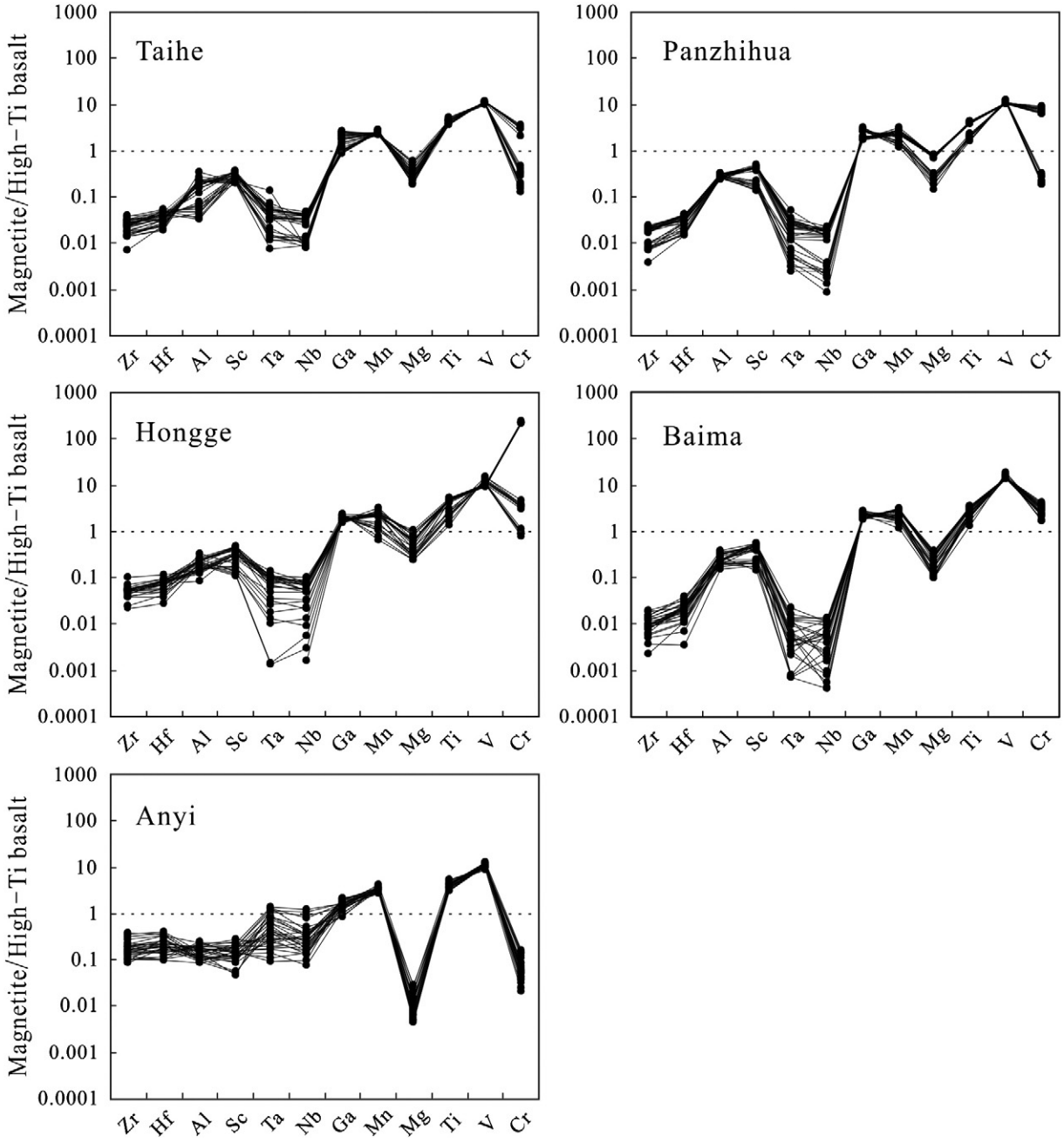

Fig. 6. Normalized multi-element variation patterns for lithophile elements in magnetite of Fe–Ti oxide ores in Taihe, Panzhihua, Hongge, Baima and Anyi intrusions. Normalized to Emeishan high-Ti basalt using average values from data published by Xiao et al. (2004), Qi and Zhou (2008) and Wang et al. (2007).

from the Hongge intrusion has the highest MgO (4.49–9.51 wt.%) and lowest FeO (33.6–40.8 wt.%) contents (Table 2). TiO_2 and V_2O_3 contents of ilmenite from the Taihe, Panzhihua, Hongge, Baima and Anyi deposits are similar and vary from 50 to 56 wt.% and from 0.4 to 0.5 wt.%, respectively.

6. Discussion

6.1. Controls on compositions of magnetite from the oxide-bearing intrusions

Trace element concentrations and their behavior in high-temperature magmatic magnetite have previously been investigated (e.g. Dare et al., 2012; Duncan and Taylor, 1968; Gao et al., 2013; Nielsen and Beard, 2000; Schock, 1979; Toplis and Corgne, 2002). Factors that control the concentrations of trace elements incorporated in magmatic magnetite include magma composition, magnetite crystallography, coexisting minerals, oxygen fugacity, temperature, cooling rate, sulfur fugacity, and silica activity (Buddington and Lindsley, 1964; Dare et al., 2012; Frost and Lindsley, 1991; Ghiorso and Sack, 1991; Toplis and Corgne, 2002). Magmatic magnetite crystallized from evolving silicate, sulfide or Fe–Ti–(P)-rich melts will incorporate a range of trace elements from divalent metals such as Mn, Zn, Co, and Ni through trivalent Cr, V, Ga and Nb, to high field strength elements (Ti, Hf, Zr, Ta, Nb) and Ge (Bragg, 1915). The substitution is mainly controlled by similarity of the ionic radius and the overall charge balance (Fig. 9). Besides, oxygen fugacity, magma composition and coexisting minerals are the dominant controlling factors. In the following section, we discuss these main factors that could affect the trace element partitioning of magnetite from oxide-bearing intrusions of the ELIP.

Table 1
LA-ICP-MS results for major and trace elements in magnetite of Fe–Ti oxide ores from the Taihe, Panzhihua, Hongge, Baima and Anyi deposits in the ELIP.

Deposit	Taihe deposit																							
Sample	TH11-7											TH11-10												
Point no.	1	2	3	4	5	6	7	8	9	10	11	1	2	3	4	5	6	7	8	9	10	11	12	13
FeO (wt.%)	78.2	77.7	78.8	79.8	78.7	77.6	75.8	77.3	78.5	79.9	78.6	78.2	78.3	78.4	76.3	76.5	75.4	78.6	79.0	78.8	78.5	76.4	75.4	74.1
TiO_2	16.8	16.7	17.3	17.1	17.4	18.5	19.4	19.3	17.1	17.0	18.2	17.4	16.6	16.8	17.1	16.9	16.8	16.1	15.8	15.9	16.1	16.5	16.7	17.0
Mg (ppm)	7517	8047	9421	5830	5321	5699	6641	6592	9309	6716	5528	7307	6389	7051	11,495	11,515	12,826	6692	8019	7134	9678	13,056	15,009	16,781
27Al	3426	4465	4738	2456	2324	2597	3680	3817	5586	3084	4220	8249	13,041	11,021	10,843	11,055	15,693	13,311	12,284	10,779	13,117	12,356	13,864	15,701
28Si	962	1376	879	702	527	1010	1727	1754	2259	626	703	1300	465	658	5967	5849	6811	2041	1405	4150	440	6720	7803	9065
40Ca	259	225	192	475	471	376	430	305	253	391	347	233	159	105	201	147	183	179	151	128	158	141	206	84.1
45Sc	7.48	5.47	6.79	6.07	7.33	7.43	6.58	8.17	7.86	7.80	8.87	9.58	8.21	9.36	8.37	8.29	9.42	9.18	9.83	8.23	8.58	9.36	9.23	9.51
51V	3465	3873	3675	3905	3795	3780	3939	3819	3689	3638	3923	3642	3683	3676	3800	3834	4046	3859	3836	3930	3792	3839	3873	3818
53Cr	22.7	21.4	23.0	21.7	29.3	21.0	20.2	22.4	25.9	22.1	18.8	8.13	10.9	10.6	9.82	11.4	12.5	11.1	9.60	11.9	8.45	12.6	11.9	12.5
55Mn	3144	3119	3301	3167	3202	3477	3514	3485	3247	3112	3230	2955	2972	2976	3019	2767	2818	2985	3021	2862	3138	2877	2878	2929
59Co	28.0	24.3	18.7	24.7	22.0	21.4	18.0	17.0	26.5	24.3	26.5	68.2	88.3	55.4	70.4	33.2	58.4	63.1	71.2	67.8	56.4	46.0	46.2	60.4
60Ni	70.7	73.0	83.7	78.6	75.0	82.4	80.3	84.1	83.1	88.6	88.6	234	263	189	130	121	137	184	160	133	150	123	118	123
65Cu	6.78	0.96	1.31	0.79	26.7	2.39	0.88	1.84	3.21	0.00	2.61	141	83.1	118	22.3	10.3	42.0	101	74.6	18.7	19.2	20.4	87.3	29.9
66Zn	191	264	217	238	232	199	91.4	186	228	209	856	416	585	559	126	199	485	693	666	532	460	172	125	538
71Ga	22.6	23.2	24.4	23.8	24.7	23.2	19.6	20.8	20.9	20.1	38.6	35.9	42.7	40.5	23.9	27.3	35.4	46.2	46.9	41.9	47.9	27.4	31.2	32.2
74Ge	0.40	0.41	0.46	0.50	0.55	0.61	0.14	0.45	0.49	0.60	0.52	0.32	0.65	0.81	0.53	0.59	0.51	0.41	0.38	0.94	0.59	0.56	0.41	0.82
88Sr	29.7	19.2	25.1	36.0	34.0	31.3	33.0	32.2	29.7	32.1	33.8	18.4	19.5	17.1	15.6	21.7	22.9	13.8	18.9	14.5	15.3	19.7	20.7	18.8
89Y	0.25	0.21	0.12	0.14	0.14	0.19	0.16	0.18	0.35	0.29	0.36	0.66	0.13	0.11	0.04	0.03	0.06	0.29	0.19	0.04	0.03	0.06	0.03	0.02
90Zr	7.90	7.68	7.44	7.54	8.08	10.20	10.51	11.49	8.36	7.66	7.12	9.59	6.78	7.18	9.19	9.17	12.37	8.73	7.97	9.60	8.76	9.69	9.40	9.71
93Nb	1.30	1.19	1.42	1.26	1.39	1.54	1.72	1.55	1.51	1.38	1.37	1.09	0.98	0.88	1.24	0.94	1.22	1.01	1.06	1.51	1.20	1.23	1.19	1.29
95Mo	0.10	0.12	0.31	0.02	0.05	0.08	0.05	0.10	0.18	0.08	0.15	0.05	0.13	0.02	0.21	0.07	0.16	0.12	0.25	0.09	0.13	0.04	0.02	0.32
111Cd	0.09	0.03	0.06	0.00	0.00	0.00	0.03	0.00	0.03	0.06	0.05	0.00	0.07	0.10	0.16	0.10	0.00	0.00	0.00	0.00	0.07	0.00	0.00	0.00
115In	0.08	0.06	0.08	0.24	0.05	0.03	0.05	0.04	0.09	0.03	0.10	0.08	0.13	0.06	0.07	0.12	0.08	0.05	0.07	0.07	0.12	0.05	0.08	0.06
118Sn	1.03	0.97	0.78	1.17	1.48	1.18	0.99	1.37	1.30	0.92	1.35	1.46	1.86	1.68	1.05	1.47	1.24	1.69	2.01	1.40	1.56	1.29	1.40	1.41
137Ba	8.37	5.41	6.10	9.87	12.61	7.70	8.92	7.80	9.91	8.25	9.22	6.66	11.6	7.11	9.52	10.5	12.6	7.85	8.94	9.54	7.99	11.7	10.4	10.7
178Hf	0.38	0.36	0.33	0.41	0.34	0.31	0.39	0.43	0.29	0.26	0.36	0.33	0.28	0.27	0.26	0.24	0.31	0.28	0.31	0.30	0.32	0.31	0.26	0.37
181Ta	0.12	0.09	0.10	0.08	0.13	0.13	0.15	0.12	0.13	0.12	0.14	0.09	0.10	0.09	0.17	0.10	0.08	0.08	0.13	0.08	0.09	0.10	0.08	0.14
182W	0.03	0.02	0.01	0.10	0.04	0.05	0.08	0.11	0.00	0.06	0.03	0.01	0.01	0.00	0.10	0.01	0.01	0.03	0.01	0.01	0.10	0.05	0.08	0.09
208Pb	0.53	0.51	0.66	0.41	0.31	0.52	0.18	0.57	0.38	0.37	0.53	1.42	2.04	1.55	0.44	0.73	0.66	1.28	1.32	1.00	1.39	0.53	0.47	0.57
209Bi	0.04	0.03	0.09	0.03	0.01	0.01	0.02	0.02	0.06	0.04	0.09	0.14	0.07	0.03	0.07	0.07	0.05	0.03	0.04	0.02	0.08	0.07	0.04	0.03

Deposit	Taihe deposit												Panzhihua deposit										
Sample	TH11-1												PZ2-1										
Point no.	1	2	3	4	5	6	7	8	9	10	11	12	1	2	3	4	5	6	7	8	9	10	11
FeO (wt.%)	80.0	81.4	80.8	78.2	81.5	81.1	79.0	78.6	79.0	77.3	78.1	80.5	76.1	76.0	75.8	75.7	76.1	76.1	75.5	76.1	76.6	76.3	76.2
TiO_2	14.1	13.4	13.8	15.4	12.9	13.2	14.7	14.8	14.4	14.0	14.2	13.8	15.0	14.9	14.9	15.2	14.9	15.4	15.0	15.0	14.7	14.5	14.3
Mg (ppm)	8838	5576	7052	6451	7388	7167	11,395	11,054	10,093	16,039	15,703	9445	22,097	22,687	23,289	22,969	22,934	22,210	23,308	21,993	22,295	22,511	23,751
27Al	16,178	15,212	14,539	16,545	14,915	14,953	16,059	15,964	14,308	24,278	18,394	14,698	20,473	20,549	21,694	20,768	20,445	18,507	21,972	19,923	19,860	21,525	22,136
28Si	525	1031	586	2504	511	1530	424	1654	2534	615	1124	464	579	562	486	643	471	445	585	627	464	609	507
40Ca	120	135	163	152	226	211	30.1	118	147	111	126	159	6.70	0.00	0.00	0.00	0.00	0.00	5.74	0.00	0.00	74.1	0.00
45Sc	6.12	6.16	6.05	6.69	5.43	5.81	6.01	5.92	5.41	5.58	6.23	6.98	10.9	11.5	11.8	13.2	12.0	11.8	11.0	11.4	12.6	11.1	11.7
51V	4138	4046	4084	4250	4176	4200	3970	4063	4100	4006	4126	3914	3804	3749	3738	3753	3804	3912	3839	3950	3805	3891	3758
53Cr	222	213	199	193	197	160	214	226	192	191	199	130	421	404	407	414	410	425	450	440	414	425	408
55Mn	2941	2895	2970	3154	2748	2763	2989	3137	2930	2914	3033	3131	3010	3676	2775	3055	2966	3283	3381	3949	2785	3054	2722
59Co	91.5	81.6	78.6	88.7	118	105	100	106	75.7	99.4	90.8	89.1	229	196	235	232	236	227	177	205	225	153	235

60Ni	108	98.8	102	88.0	101	110	106	112	110	102	100	106	100	102	96.2	97.4	96.6	101	100	95.6	87.5	94.3	94.8
65Cu	110	2.11	770	3092	72.8	213	0.50	5.06	3157	5.89	157	0.99	0.66	1.64	1.19	0.92	0.61	2.03	1.23	0.39	0.86	1.41	0.81
66Zn	796	663	645	418	1386	1182	985	806	586	1005	792	732	376	490	394	405	395	382	485	455	369	497	443
71Ga	59.7	49.6	49.4	50.4	59.5	50.9	56.1	54.8	46.1	58.2	58.8	54.9	43.6	45.4	41.3	41.4	41.3	40.9	45.7	42.9	40.3	46.2	42.0
74Ge	0.80	0.77	0.63	0.57	0.26	0.69	0.82	0.53	0.82	0.77	0.98	0.39	0.48	0.72	0.62	0.52	0.39	0.60	0.86	0.75	0.65	0.50	0.48
88Sr	9.81	9.89	10.1	10.0	15.5	16.4	10.7	8.86	9.92	8.23	10.2	7.12	0.05	0.06	0.02	0.01	0.02	0.04	0.00	0.03	0.02	0.05	0.00
89Y	0.07	0.30	0.23	0.06	0.06	0.02	0.00	0.00	0.07	0.01	0.00	0.20	0.01	0.10	0.00	0.01	0.00	0.00	0.02	0.00	0.01	0.08	0.00
90Zr	2.24	4.55	4.39	5.82	4.72	5.06	5.63	4.87	4.64	4.41	4.21	5.49	5.65	6.12	6.77	6.96	6.21	6.49	6.04	5.31	7.18	5.76	6.06
93Nb	0.29	0.28	0.29	0.40	0.32	0.36	0.34	0.43	0.50	0.46	0.37	0.33	0.52	0.58	0.72	0.61	0.62	0.75	0.62	0.74	0.79	0.52	0.67
95Mo	0.08	0.06	0.14	0.10	0.06	0.51	0.19	0.07	0.00	0.22	0.10	0.08	0.09	0.24	0.07	0.04	0.05	0.16	0.04	0.11	0.00	0.15	0.24
111Cd	0.04	0.03	0.15	0.07	0.07	0.03	0.07	0.00	0.00	0.04	0.11	0.03	0.09	0.15	0.12	0.17	0.03	0.01	0.13	0.40	0.18	0.00	0.19
115In	0.14	0.10	0.06	0.09	0.09	0.07	0.18	0.13	0.06	0.09	0.07	0.07	0.09	0.10	0.14	0.07	0.10	0.11	0.09	0.10	0.20	0.12	0.09
118Sn	1.67	1.62	1.33	1.38	2.01	2.23	2.19	2.09	1.24	1.77	1.49	1.63	1.77	1.03	1.59	1.67	1.01	1.43	1.58	1.53	1.47	1.62	1.20
137Ba	11.1	11.0	6.45	11.5	21.5	20.7	8.87	7.57	10.3	11.9	10.2	14.4	0.16	0.00	0.00	0.00	0.00	0.02	0.02	0.04	0.00	0.00	0.04
178Hf	0.19	0.22	0.25	0.24	0.21	0.18	0.26	0.21	0.19	0.16	0.15	0.19	0.28	0.24	0.25	0.27	0.30	0.32	0.26	0.31	0.31	0.30	0.31
181Ta	0.33	0.04	0.03	0.03	0.02	0.04	0.09	0.04	0.03	0.04	0.03	0.05	0.07	0.12	0.05	0.06	0.08	0.05	0.07	0.03	0.09	0.04	0.07
182W	0.02	0.01	0.01	0.01	0.03	0.01	0.05	0.05	0.06	0.25	0.02	0.01	0.00	0.00	0.00	0.07	0.01	0.00	0.00	0.01	0.07	0.01	0.01
208Pb	1.21	1.45	2.05	1.25	1.92	1.48	1.25	1.18	1.30	1.23	1.03	1.46	0.05	0.12	0.03	0.01	0.04	0.03	0.03	0.03	0.16	0.05	0.04
209Bi	0.05	0.05	0.04	0.07	0.05	0.01	0.12	0.05	0.04	0.03	0.05	0.01	0.02	0.05	0.03	0.07	0.08	0.07	0.07	0.03	0.02	0.09	0.03

Deposit	Panzhihua deposit																						
Sample	PZ2-2											PZ1											
Point no.	1	2	3	4	5	6	7	8	9	10	11	1	2	3	4	5	6	7	8	9	10	11	12
FeO (wt.%)	76.0	77.0	76.5	75.4	75.7	75.9	76.8	76.1	76.9	75.7	75.5	87.4	86.3	85.1	86.2	87.0	86.0	85.8	85.8	86.1	85.8	87.8	88.4
TiO_2	14.5	14.6	15.3	15.6	15.4	15.7	14.4	15.9	15.2	15.8	15.3	6.39	7.31	8.54	7.19	7.58	7.36	7.47	8.18	7.59	7.66	6.18	5.93
Mg (ppm)	22,905	20,851	22,317	22,357	22,327	21,351	21,092	20,021	20,639	22,007	23,087	7617	8133	8882	5460	4165	9069	7485	6962	8350	6571	7961	5778
27Al	21,999	18,346	16,173	20,102	19,641	17,976	20,134	16,919	16,518	17,845	20,141	19,154	19,605	18,698	20,275	18,504	19,858	19,931	18,320	19,479	21,390	18,147	17,814
28Si	1138	1020	988	919	822	779	1039	681	700	745	754	948	1049	1038	3852	852	935	2536	1360	731	1354	935	919
40Ca	36.1	0.00	39.9	54.4	11.2	167	55.0	110	0.00	29.4	25.4	85.5	3.60	0.00	125	16.6	4.52	55.0	0.00	0.00	106	0.00	54.4
45Sc	11.4	10.9	11.9	12.5	12.6	12.3	9.97	12.6	11.7	12.4	12.2	3.92	6.08	4.83	6.21	3.79	4.75	4.97	5.53	4.68	4.22	4.33	3.97
51V	3836	3896	3804	3805	3702	3760	3852	3823	3752	3846	3810	4508	3918	3960	3998	3938	4326	4282	4153	4149	4217	4299	4428
53Cr	496	489	505	515	528	573	526	493	556	567	600	12.2	13.3	13.3	11.9	12.7	14.4	17.7	12.9	14.1	18.1	18.2	20.4
55Mn	3587	3390	2873	3443	3497	3211	3162	3092	2766	3161	3548	1673	2403	2430	1479	2106	2065	1718	2065	2091	1938	1711	1814
59Co	160	200	160	118	220	122	135	167	216	161	87.0	107	165	174	88.1	138	145	104	128	140	139	133	145
60Ni	83.6	91.2	101	85.4	85.3	84.4	76.2	73.7	86.8	95.5	84.3	7.02	8.61	10.1	7.89	7.77	7.12	7.31	7.26	9.11	10.4	9.09	10.4
65Cu	0.22	0.13	5.76	6.96	1.68	16.3	3.76	16.5	0.46	5.84	2.24	0.40	0.00	0.75	60.6	6.35	0.65	33.5	3.25	1.23	3.23	0.90	1.31
66Zn	482	408	381	499	396	512	498	484	299	440	519	606	422	527	724	499	500	759	471	482	713	426	376
71Ga	44.2	40.0	46.7	43.8	43.2	45.2	45.4	42.3	40.3	44.8	44.6	72.7	64.3	59.7	66.6	65.6	60.9	61.5	60.2	61.9	67.1	62.3	64.5
74Ge	0.57	0.52	0.91	0.57	0.72	0.53	0.59	0.55	0.54	0.90	0.43	0.95	1.03	0.98	0.86	0.77	0.72	1.18	1.16	0.91	1.24	0.91	0.64
88Sr	0.12	0.12	1.27	0.53	0.09	0.19	0.13	0.22	0.00	0.38	0.10	0.37	0.03	0.03	2.06	0.07	0.00	1.74	0.85	0.03	0.68	0.07	0.80
89Y	0.00	0.01	0.00	0.00	0.01	0.02	0.01	0.02	0.01	0.01	0.06	0.01	0.00	0.01	0.03	0.09	0.01	0.03	0.00	0.01	0.00	0.02	0.00
90Zr	5.68	6.08	6.14	7.01	6.80	6.97	5.67	6.94	7.35	6.50	5.79	1.15	2.33	2.31	3.06	2.58	2.29	2.96	3.10	2.31	3.08	2.48	2.18
93Nb	0.52	0.49	0.57	0.49	0.74	0.62	0.42	0.68	0.55	0.62	0.63	0.06	0.03	0.14	0.07	0.12	0.12	0.08	0.05	0.07	0.09	0.09	0.00
95Mo	0.02	0.36	0.16	0.14	0.13	0.14	0.09	0.06	0.16	0.08	0.12	0.57	0.27	0.38	0.41	1.38	0.28	0.24	0.26	0.19	0.35	0.18	0.19
111Cd	0.00	0.03	0.11	0.00	0.03	0.00	0.04	0.14	0.00	0.00	0.07	0.03	0.06	0.18	0.00	0.22	0.06	0.03	0.00	0.00	0.03	0.12	0.13
115In	0.10	0.08	0.12	0.09	0.09	0.19	0.11	0.12	0.08	0.14	0.09	0.11	0.13	0.07	0.11	0.06	0.12	0.09	0.07	0.14	0.09	0.17	0.06
118Sn	1.23	1.56	1.38	1.74	1.89	1.68	1.26	1.66	1.30	1.37	1.87	1.03	1.60	1.27	1.51	1.08	1.51	1.33	1.23	1.43	1.76	1.33	1.75
137Ba	0.16	0.04	0.14	0.12	0.00	0.02	0.02	0.00	0.00	0.00	0.32	0.02	0.00	0.04	0.62	0.10	0.00	0.53	0.45	0.00	0.23	0.12	0.58
178Hf	0.28	0.24	0.25	0.32	0.25	0.34	0.23	0.20	0.31	0.26	0.33	0.11	0.13	0.22	0.14	0.12	0.12	0.23	0.20	0.16	0.16	0.20	0.12
181Ta	0.06	0.03	0.06	0.07	0.06	0.06	0.03	0.08	0.04	0.05	0.07	0.01	0.01	0.03	0.02	0.03	0.02	0.01	0.01	0.01	0.01	0.01	0.00
182W	0.01	0.01	0.00	0.15	0.00	0.00	0.08	0.06	0.01	0.07	0.24	0.01	0.00	0.01	0.02	0.14	0.01	0.00	0.00	0.01	0.01	0.24	0.01
208Pb	0.04	0.02	0.05	0.07	0.01	0.03	0.09	0.06	0.02	0.02	0.03	0.05	0.02	0.02	0.09	0.04	0.04	0.04	0.02	0.04	0.03	0.03	0.03
209Bi	0.00	0.10	0.13	0.02	0.01	0.06	0.04	0.83	0.00	0.11	0.09	0.08	0.06	0.01	0.09	0.05	0.03	0.07	0.08	0.05	0.02	0.08	0.06

(continued on next page)

Table 1 (*continued*)

Deposit	Hongge deposit																				
Sample	HG11-35										HG11-21										
Point no.	1	2	3	4	5	6	7	8	9	10	1	2	3	4	5	6	7	8	9	10	
FeO (wt.%)	90.0	81.8	88.8	84.9	82.0	84.2	83.4	78.7	86.8	86.2	75.0	78.5	76.1	75.9	77.1	76.1	74.6	76.4	75.5	75.1	
TiO_2	4.84	8.31	5.81	8.72	10.0	9.55	11.3	16.5	7.7	8.8	18.0	17.3	17.3	17.8	17.8	17.7	18.8	17.4	19.0	19.1	
Mg (ppm)	6661	7773	6984	8787	12,740	10,759	8352	8702	7911	8290	18,825	7497	18,882	17,722	11,566	17,217	18,438	16,857	14,582	16,395	
27Al	12,847	11,722	13,995	17,272	22,148	14,814	12,590	10,321	14,272	10,920	12,037	5685	10,035	10,484	9439	9678	10,962	10,682	8532	9107	
28Si	2079	1359	1620	2113	2825	1738	1944	1567	1531	1595	1252	1253	992	821	551	942	757	881	802	590	
40Ca	2.43	51.6	160	409	427	108	7.06	4.58	0.00	154	230	2963	319	217	297	198	275	192	211	191	
45Sc	2.83	3.99	3.14	3.53	5.18	3.82	4.30	6.95	3.28	4.66	9.48	9.12	8.07	8.35	8.70	7.44	9.52	8.67	8.60	8.61	
51V	5303	4361	4748	4134	3900	5189	4103	3700	4280	4560	3584	3552	3783	3698	3634	3669	3679	3887	3571	3628	
53Cr	302	203	224	215	214	248	224	191	230	249	56.7	49.9	54.4	54.6	54.3	63.5	55.5	69.5	55.6	59.3	
55Mn	818	1337	965	1515	1699	1356	1889	2597	1341	1498	2770	3052	2664	2833	3153	2838	3033	2608	3083	2791	
59Co	117	102	79.0	152	131	138	123	126	121	126	177	85.2	162	148	152	173	169	122	109	120	
60Ni	233	209	255	291	221	251	278	236	293	329	159	214	267	162	172	152	203	130	153	121	
65Cu	6.94	1.09	366	9.59	39.6	2.14	217	1.99	0.30	59.5	55.8	25.8	26.1	21.2	27.0	15.5	43.7	49.1	25.7	13.3	
66Zn	221	248	452	547	678	416	358	265	315	395	967	959	1134	1028	898	982	1117	907	1002	822	
71Ga	53.0	45.3	49.4	49.7	51.2	46.8	44.9	39.4	52.1	46.0	53.8	36.2	45.7	43.8	38.1	41.3	48.0	44.6	42.4	45.5	
74Ge	0.53	0.27	0.60	0.61	0.59	0.56	0.71	0.27	0.41	0.77	1.18	0.38	0.43	0.63	0.44	0.32	0.31	0.68	0.43	0.61	
88Sr	0.16	0.12	2.25	1.75	3.18	0.99	0.12	0.14	0.24	1.54	25.70	25.6	20.3	15.7	15.5	17.1	20.2	20.6	16.6	22.2	
89Y	0.10	0.06	0.10	0.07	0.07	0.13	0.18	0.03	0.06	0.05	0.02	0.54	0.07	0.03	0.19	0.08	0.04	0.18	0.07	0.04	
90Zr	6.49	11.4	7.74	15.0	15.6	17.0	17.1	30.2	11.3	12.5	16.0	14.6	16.3	17.9	18.2	15.8	17.7	13.7	17.0	17.1	
93Nb	0.11	0.79	0.19	0.46	0.76	1.68	1.11	2.88	0.32	0.06	2.86	2.72	2.50	2.61	2.96	2.37	2.58	1.99	3.10	2.80	
95Mo	0.69	0.24	0.51	0.41	0.44	0.39	0.43	0.40	0.41	0.22	0.32	0.17	0.08	0.23	0.22	0.15	0.12	0.31	0.26	0.27	
111Cd	0.11	0.08	0.03	0.00	0.00	0.00	0.11	0.17	0.20	0.03	0.00	0.08	0.00	0.00	0.00	0.00	0.00	0.16	0.00	0.00	
115In	0.56	0.07	0.18	0.07	0.11	2.29	0.07	0.08	0.11	0.09	0.21	0.11	0.15	0.14	0.11	0.10	0.12	0.12	0.09	0.12	
118Sn	3.26	2.84	2.99	3.25	3.30	3.35	2.63	2.56	3.03	3.15	4.10	1.96	2.24	2.79	2.51	2.34	2.19	3.15	3.00	2.50	
137Ba	0.14	0.06	0.72	0.80	0.90	0.74	0.14	0.00	0.10	0.66	8.50	5.97	8.08	6.00	6.21	5.86	7.13	6.61	6.25	7.24	
178Hf	0.22	0.46	0.33	0.39	0.42	0.64	0.46	0.89	0.29	0.37	0.69	0.57	0.61	0.61	0.60	0.60	0.67	0.54	0.63	0.64	
181Ta	0.00	0.04	0.00	0.03	0.08	0.12	0.06	0.18	0.03	0.00	0.34	0.25	0.20	0.27	0.22	0.22	0.26	0.15	0.23	0.24	
182W	0.04	0.06	0.15	0.05	0.07	0.01	0.07	0.07	0.06	0.01	0.32	0.13	0.12	0.16	0.10	0.09	0.18	0.13	0.31	0.17	
208Pb	0.51	0.15	1.25	0.98	0.54	0.27	0.42	0.22	0.47	0.71	0.09	0.03	0.06	0.05	0.43	0.04	0.08	0.03	0.06	0.04	
209Bi	0.12	0.00	0.08	0.04	0.06	0.08	0.04	0.03	0.15	0.13	0.89	1.10	0.71	0.63	0.66	0.62	0.86	0.51	0.71	0.58	

Deposit	Hongge deposit									Anyi deposit															
Sample	HG11-27									AY11-37								AY11-80							
Point no.	1	2	3	4	5	6	7	8	9	1	2	3	4	5	6	7	8	1	2	3	4	5	6	7	8	9
FeO (wt.%)	68.4	71.3	70.5	71.5	71.4	71.4	71.5	72.5	75.0	82.3	83.6	82.9	82.8	83.0	75.8	83.6	79.7	81.6	83.3	84.5	85.1	83.2	81.9	82.7	81.1	81.3
TiO_2	19.6	17.5	18.4	17.9	17.7	17.4	17.5	17.1	15.5	13.6	12.4	12.9	13.3	12.8	19.2	11.6	16.6	13.9	12.3	11.0	11.5	13.6	14.6	13.8	15.5	15.2
Mg (ppm)	29,850	26,233	26,878	22,896	23,076	26,740	26,508	23,223	18,046	809	268	235	397	187	748	452	411	387	445	612	195	192	148	572	277	233
27Al	19,000	17,092	16,421	16,699	17,885	16,809	15,909	15,559	13,708	10,689	11,077	11,832	11,248	13,614	15,774	15,762	10,551	12,155	13,112	12,264	8329	7833	10,075	8935	7568	8171
28Si	1017	870	771	847	832	823	769	722	721	2024	1180	1259	1459	1160	1354	1271	1284	1368	1512	2050	1415	1323	1332	2116	1220	1339
40Ca	113	0.00	183	36.0	0.00	0.00	0.00	27.4	48.5	90.6	123	132	147	90.6	122	21.2	90.3	52.8	60.3	282	391	5.55	20.6	67.4	34.3	212
45Sc	12.5	11.6	12.7	11.1	12.2	10.5	11.4	12.8	12.1	2.97	4.27	4.10	3.15	2.90	6.38	3.92	5.31	4.44	4.96	3.89	2.84	2.92	1.25	2.34	5.31	3.10
51V	3320	3439	3289	3349	3314	3298	3273	3389	3652	3587	3995	4114	3656	3640	3087	3718	3166	3582	4010	4430	3856	3587	3417	3803	4026	4114
53Cr	13,841	14,122	14,121	14,501	14,667	14,472	14,423	14,852	15,596	3.76	3.14	4.38	3.44	2.79	2.47	5.43	1.31	3.41	9.04	10.2	8.19	9.47	5.55	8.81	6.97	4.84
55Mn	2785	3247	2980	3248	3629	3372	3248	3196	4054	3637	3393	3599	3614	3483	5241	3358	4499	4236	3895	3500	3543	4190	4464	4116	4633	4474
59Co	263	243	239	187	171	260	232	176	122	79.3	80.5	70.4	70.0	61.0	135	130	116	126	145	141	67.3	67.72	59.8	54.2	79.2	70.7
60Ni	1236	1308	1265	1231	1230	1294	1238	1146	1282	109	99.1	101	106	66.4	119	155	114	150	193	194	168	166	82.4	103	175	139
65Cu	1.66	0.87	1.80	1.30	1.93	2.36	0.00	1.00	2.07	1.76	1.24	1.63	1.55	2.59	2.17	3.03	1.00	3.07	8.61	3.26	2.66	2.08	1.71	1.40	4.18	4.10
66Zn	437	529	507	681	696	579	510	560	717	2631	2470	2443	2038	1442	2271	2262	1541	4606	2559	2451	1177	1528	547	27.1	2049	1713
71Ga	37.3	41.7	39.5	39.7	38.1	39.6	36.0	35.4	40.9	44.2	41.5	41.8	37.2	34.7	39.2	47.8	38.5	46.1	49.7	49.0	30.9	32.9	23.5	21.0	39.1	31.3
74Ge	1.03	0.48	0.76	0.43	0.72	0.78	0.39	0.09	0.55	0.34	0.41	0.75	0.35	0.48	0.43	0.48	0.37	0.69	0.52	0.08	0.34	0.58	0.60	0.50	0.35	0.42
88Sr	0.12	0.15	0.30	0.09	0.08	0.15	0.05	0.08	0.18	1.23	0.28	1.58	2.22	6.03	1.92	0.93	0.06	0.06	0.17	3.09	1.74	0.16	1.93	11.53	0.03	0.24
89Y	0.01	0.00	0.00	0.01	0.00	0.00	0.01	0.02	0.01	0.02	0.01	0.02	0.00	0.06	0.00	0.00	0.02	0.00	0.02	0.03	0.06	0.00	0.01	0.01	0.01	0.03

90Zr	21.3	16.7	19.6	16.6	16.5	16.0	16.1	16.9	13.3	63.8	53.5	40.3	39.1	61.7	69.1	31.6	112	59.0	50.3	70.2	51.9	59.1	48.3	45.1	86.3	97.7
93Nb	3.52	1.72	2.40	2.65	1.75	1.81	1.86	1.89	1.17	8.47	4.57	6.75	5.26	5.32	44.15	3.52	28.6	12.9	7.07	5.12	6.02	11.0	15.1	9.74	37.0	31.4
95Mo	0.21	0.04	0.59	0.04	0.15	0.11	0.13	0.34	0.54	2.70	3.28	2.29	2.07	2.63	1.27	2.57	1.65	1.50	1.32	1.85	3.74	2.78	2.27	1.91	2.04	2.66
111Cd	0.18	0.44	0.16	0.00	0.25	0.20	0.00	0.03	0.24	0.12	0.00	0.30	0.00	0.03	0.00	0.14	0.00	0.00	0.13	0.00	0.09	0.09	0.00	0.06	0.03	0.27
115In	0.10	0.18	0.14	0.10	0.12	0.15	0.09	0.12	0.13	0.12	0.06	0.05	0.02	0.03	0.03	0.09	0.04	0.05	0.04	0.03	0.03	0.03	0.08	0.01	0.07	0.04
118Sn	2.94	2.73	2.79	2.99	2.17	2.62	2.35	2.14	3.05	5.17	5.07	6.06	5.13	5.59	4.21	4.64	4.97	4.45	4.84	5.76	5.48	4.90	5.94	3.17	6.69	5.58
137Ba	0.03	0.03	0.17	0.00	0.03	0.09	0.09	0.06	0.03	0.24	0.00	0.27	0.42	1.64	0.14	0.42	0.00	0.05	0.44	0.50	0.40	0.00	0.09	2.01	0.00	0.29
178Hf	0.73	0.66	0.72	0.67	0.59	0.55	0.53	0.71	0.64	2.11	1.47	1.25	1.16	1.70	2.69	0.80	3.07	1.82	1.48	1.50	1.68	2.04	2.06	1.31	2.66	2.94
181Ta	0.27	0.17	0.25	0.19	0.21	0.26	0.23	0.16	0.09	1.13	0.41	0.45	0.60	0.90	3.43	0.22	3.14	2.20	0.90	0.27	1.33	1.99	3.08	0.71	2.81	2.58
182W	0.05	0.01	0.12	0.02	0.01	0.02	0.21	0.02	0.12	0.19	0.11	0.16	0.08	0.04	0.08	0.04	0.28	0.11	0.00	0.04	0.11	0.03	0.15	0.21	0.05	0.07
208Pb	0.05	0.17	0.03	0.02	0.05	0.07	0.02	0.01	0.08	0.06	0.02	0.08	0.02	0.01	0.03	0.03	0.01	0.03	0.09	0.07	0.03	0.03	0.02	0.05	0.03	0.03
209Bi	0.11	0.12	0.17	0.06	0.02	0.06	0.07	0.05	0.10	1.36	0.23	0.77	2.78	1.10	1.48	0.18	0.09	0.05	0.00	1.11	0.40	0.18	0.66	3.51	0.17	0.10

Deposit	Anyi deposit													Baima deposit							
Sample	AY11-40													BM12-127							
Point no.	1	2	3	4	5	6	7	8	9	10	11	12	13	1	2	3	4	5	6	7	8
FeO (wt.%)	79.0	81.3	82.3	80.1	77.4	77.1	80.1	80.7	81.5	80.9	80.5	79.4	79.6	87.7	87.7	87.8	87.7	85.7	88.0	87.1	86.1
TiO_2	16.3	13.8	14.6	16.6	18.9	19.2	16.8	16.4	15.6	15.9	14.6	17.3	15.3	7.47	8.14	7.63	6.16	9.51	7.42	7.77	9.10
Mg (ppm)	375	342	131	617	274	210	187	149	141	228	150	162	395	3194	2799	3086	4844	3550	3001	3151	3505
27Al	13,832	13,677	7218	6538	8723	10,028	6749	6592	6206	6782	17,563	7659	13,972	14,617	11,835	13,766	19,025	13,637	13,515	14,931	14,252
28Si	1190	1304	1144	2574	1346	1224	1319	1335	1279	1450	1325	1294	1263	796	826	773	697	793	954	765	702
40Ca	56.3	22.3	55.7	144.1	50.9	63.1	125.7	36.2	74.7	2.71	53.6	97.1	153	0.00	0.00	0.00	49.1	34.1	11.4	34.7	0.00
45Sc	6.72	5.39	1.52	1.41	5.34	5.95	3.96	4.13	2.89	3.53	3.68	2.42	7.38	5.09	5.36	4.53	3.70	5.42	6.16	6.28	5.56
51V	3633	4190	4598	4043	3423	3533	3993	3813	4364	4347	4125	3628	3736	5033	4893	4768	5188	4900	4954	4995	4806
53Cr	3.67	3.72	2.34	1.58	2.82	4.49	2.49	2.09	3.59	4.16	2.67	3.72	3.32	244	223	238	260	233	193	200	239
55Mn	4552	4020	3894	4316	4749	4802	4535	4428	4133	4297	4125	4856	4568	2160	2188	1840	2026	2604	2333	2690	2507
59Co	139	131	51.2	50.3	69.1	61.7	58.7	49.6	51.8	58.1	51.3	52.6	131	122	87.8	67.0	127	113	132	157	116
60Ni	16.5	16.4	11.9	7.07	13.9	10.7	9.30	11.4	9.90	13.6	13.5	4.08	16.0	160	145	133	167	154	193	209	163
65Cu	2.92	1.27	0.97	1.41	3.16	1.29	2.08	1.34	2.30	2.08	1.52	2.39	1.93	1.16	0.25	12.6	0.14	0.24	1.19	0.00	1.68
66Zn	3725	4638	772	303	3040	1444	1447	317	624	1288	210	484	5613	228	172	416	573	159	283	170	202
71Ga	44.5	47.6	29.8	23.1	32.6	31.4	34.4	37.0	29.5	36.6	27.5	19.1	45.6	55.4	54.3	46.2	60.2	56.0	63.8	63.0	54.0
74Ge	0.33	0.27	0.05	0.31	0.51	0.33	0.43	0.58	0.33	0.58	0.65	0.45	0.59	0.50	0.57	0.76	0.84	0.56	0.67	0.80	0.91
88Sr	0.22	2.96	1.06	2.29	2.71	2.93	1.44	0.06	0.79	1.07	1.69	1.87	14.46	0.02	0.04	0.07	0.01	0.11	0.13	0.06	0.00
89Y	0.00	0.01	0.02	0.04	0.02	0.00	0.00	0.00	0.00	0.01	0.00	0.08	0.02	0.00	0.01	0.01	0.01	0.01	0.00	0.00	0.00
90Zr	47.3	42.3	47.1	27.2	58.0	37.2	116.5	27.7	31.7	44.9	32.8	58.5	33.6	3.09	3.07	5.94	3.03	3.65	2.75	2.97	2.45
93Nb	10.5	8.13	7.47	8.08	14.6	11.8	12.8	11.6	4.70	6.25	2.68	18.4	11.7	0.02	0.03	0.22	0.06	0.18	0.00	0.03	0.09
95Mo	1.92	1.61	3.99	4.47	2.09	1.69	3.05	2.91	3.42	2.92	1.26	2.78	1.82	0.38	0.49	0.41	0.43	0.49	0.69	0.37	0.53
111Cd	0.13	0.06	0.00	0.00	0.06	0.09	0.00	0.15	0.00	0.08	0.09	0.00	0.16	0.00	0.00	0.00	0.43	0.08	0.00	0.19	0.10
115In	0.09	0.13	0.02	0.04	0.07	0.04	0.21	0.08	0.03	0.03	0.03	0.05	0.06	0.11	0.04	0.04	0.07	0.12	0.08	1.06	0.13
118Sn	3.35	3.36	3.53	3.24	4.17	3.63	4.12	3.35	3.76	3.93	3.33	3.18	3.69	1.25	1.11	1.09	1.14	1.50	1.63	1.40	1.10
137Ba	1.81	0.23	0.22	0.38	0.37	0.50	0.24	0.03	0.18	0.00	0.30	0.65	3.90	0.15	0.06	0.06	0.06	0.21	0.09	0.09	0.00
178Hf	1.11	1.26	1.49	1.44	1.05	0.80	2.81	2.28	0.76	1.57	0.93	1.47	1.39	0.17	0.12	0.18	0.10	0.17	0.10	0.15	0.17
181Ta	0.66	0.46	1.05	1.52	0.83	0.62	1.78	1.54	0.66	1.02	0.33	2.02	0.56	0.01	0.00	0.01	0.00	0.01	0.00	0.01	0.02
182W	0.04	0.12	0.10	0.35	0.20	0.09	0.12	0.10	0.17	0.13	0.46	0.11	0.06	0.11	0.07	0.04	0.04	0.02	0.00	0.01	0.00
208Pb	0.02	0.11	0.03	0.03	0.06	0.02	0.01	0.03	0.02	0.02	0.01	0.04	0.01	0.08	0.03	0.15	0.02	0.14	0.01	0.04	0.01
209Bi	0.04	0.64	0.14	0.71	0.34	0.06	0.71	0.08	0.13	0.02	0.27	0.79	2.99	0.03	0.02	0.04	0.00	0.09	0.02	0.01	0.02

Deposit	Baima deposit																				
Sample	BM12-126						BM12-125								BM12-124							
Point no.	1	2	3	4	5	6	1	2	3	4	5	6	7	8	1	2	3	4	5	6	7	8
FeO (wt.%)	82.5	81.9	83.5	82.9	81.9	82.6	83.3	84.8	86.5	87.0	85.8	87.4	91.3	84.9	80.1	81.2	80.6	80.6	79.4	81.0	81.9	81.2
TiO_2	9.87	10.5	10.9	11.0	11.4	11.2	9.42	9.49	7.71	7.67	8.58	7.89	4.76	9.56	12.5	12.5	12.4	11.7	12.0	11.6	12.1	11.3
Mg (ppm)	9915	10,046	6599	7879	8710	8057	6402	4977	5560	3907	5506	3561	2787	4658	9775	8518	7791	10,304	11,089	7723	7808	9245
27Al	22,897	23,015	14,821	16,294	19,467	17,561	24,681	17,156	17,630	16,149	16,682	13,285	10,263	17,043	21,430	17,289	20,918	23,180	26,510	23,705	16,343	22,274
28Si	776	745	633	635	737	767	1010	815	689	828	754	633	795	878	907	794	939	763	990	829	734	809

(continued on next page)

Table 1 *(continued)*

Deposit	Baima deposit																				
Sample	BM12-126						BM12-125								BM12-124							
Point no.	1	2	3	4	5	6	1	2	3	4	5	6	7	8	1	2	3	4	5	6	7	8
40Ca	0.00	0.00	78.1	0.00	0.00	0.00	0.00	14.59	16.61	0.00	55.70	71.98	4.18	57.33	40.37	0.00	31.89	22.35	42.90	0.00	41.09	0.00
45Sc	11.3	9.89	12.8	13.8	13.4	13.9	12.3	11.7	6.69	11.5	11.4	11.3	4.96	10.3	13.5	14.9	14.7	11.9	14.8	11.7	14.0	12.7
51V	5010	5043	4967	5045	4908	4957	4984	5283	5580	5763	5295	5560	6308	4981	4935	4861	4851	4978	4786	4874	4959	5006
53Cr	212	212	188	186	200	187	143	152	203	103	111	109	157	141	143	132	143	139	146	145	149	174
55Mn	3521	3487	3655	3886	3748	3184	2383	2943	2357	2559	2423	2820	1492	2651	3372	3577	3998	3363	3662	3612	3431	3799
59Co	183	197	144	178	191	184	182	152	139	137	131	179	127	156	193	204	202	204	218	180	172	211
60Ni	233	236	230	250	249	243	221	195	175	186	174	259	223	213	222	231	238	240	219	247	232	235
65Cu	0.37	0.78	0.00	0.93	0.00	0.39	1.40	0.79	21.3	0.38	1.59	2.00	0.00	0.99	0.00	0.22	0.87	0.78	1.92	0.00	2.27	0.00
66Zn	413	388	176	189	271	253	481	239	288	189	331	110	107	347	355	329	184	417	485	223	189	297
71Ga	45.9	47.8	39.5	42.0	42.6	42.3	54.5	53.3	54.9	59.3	49.3	53.0	52.4	50.9	45.5	44.5	45.7	46.5	49.6	48.9	45.1	45.4
74Ge	0.82	0.76	0.45	0.87	1.11	0.40	0.64	0.53	0.60	0.69	0.81	0.69	0.91	0.52	0.73	0.68	0.95	0.67	0.73	0.93	0.97	0.68
88Sr	0.04	0.10	0.01	0.02	0.01	0.02	0.04	0.05	0.21	0.08	0.05	0.19	0.11	0.32	0.04	0.06	0.02	0.14	0.03	0.02	0.05	0.11
89Y	0.00	0.04	0.02	0.00	0.00	0.00	0.00	0.02	0.01	0.01	0.00	0.01	0.03	0.00	0.02	0.00	0.00	0.00	0.02	0.00	0.01	0.00
90Zr	3.45	3.04	2.03	2.76	2.99	3.07	2.50	1.95	1.63	0.72	4.90	1.75	1.15	2.58	6.30	4.25	2.94	4.26	4.82	2.42	2.91	4.10
93Nb	0.23	0.42	0.21	0.32	0.21	0.18	0.14	0.10	0.08	0.08	0.03	0.01	0.01	0.05	0.47	0.34	0.42	0.41	0.20	0.25	0.41	0.36
95Mo	0.07	0.23	0.02	0.22	0.08	0.41	0.86	0.16	0.33	0.41	0.23	0.64	0.84	1.08	0.12	0.08	0.08	0.13	0.00	0.04	0.27	0.12
111Cd	0.28	0.10	0.15	0.09	0.00	0.14	0.11	0.10	0.10	0.09	0.05	0.30	0.24	0.26	0.21	0.21	0.00	0.00	0.06	0.06	0.05	0.06
115In	0.12	0.16	0.10	0.08	0.09	0.12	0.06	0.17	0.18	0.16	0.10	0.14	0.12	0.10	0.13	0.34	0.13	0.11	0.11	0.09	0.10	0.06
118Sn	0.96	1.25	1.41	1.12	1.30	0.71	1.88	1.54	1.66	1.25	1.47	1.82	2.35	1.73	1.13	0.75	1.08	1.08	0.93	1.38	1.13	1.10
137Ba	0.00	0.07	0.00	0.00	0.03	0.03	0.07	0.00	0.14	0.03	0.13	0.14	0.00	0.00	0.00	0.10	0.07	0.59	0.00	0.00	0.36	0.00
178Hf	0.14	0.15	0.22	0.14	0.16	0.17	0.18	0.09	0.06	0.09	0.30	0.09	0.03	0.13	0.26	0.22	0.20	0.22	0.27	0.19	0.19	0.16
181Ta	0.01	0.04	0.01	0.01	0.00	0.02	0.01	0.00	0.01	0.01	0.01	0.01	0.00	0.03	0.03	0.03	0.02	0.03	0.03	0.00	0.05	0.01
182W	0.01	0.07	0.01	0.00	0.00	0.00	0.06	0.02	0.05	0.04	0.00	0.11	0.06	0.02	0.07	0.04	0.01	0.12	0.02	0.00	0.32	0.05
208Pb	0.00	0.01	0.07	0.01	0.04	0.02	0.02	0.03	0.04	0.02	0.05	0.09	0.04	0.18	0.02	0.04	0.00	0.04	0.27	0.02	0.03	0.06
209Bi	0.00	0.08	0.02	0.03	0.03	0.04	0.03	0.27	0.35	0.03	0.01	0.04	0.04	0.01	0.06	0.04	0.06	0.04	0.03	0.02	0.15	0.04

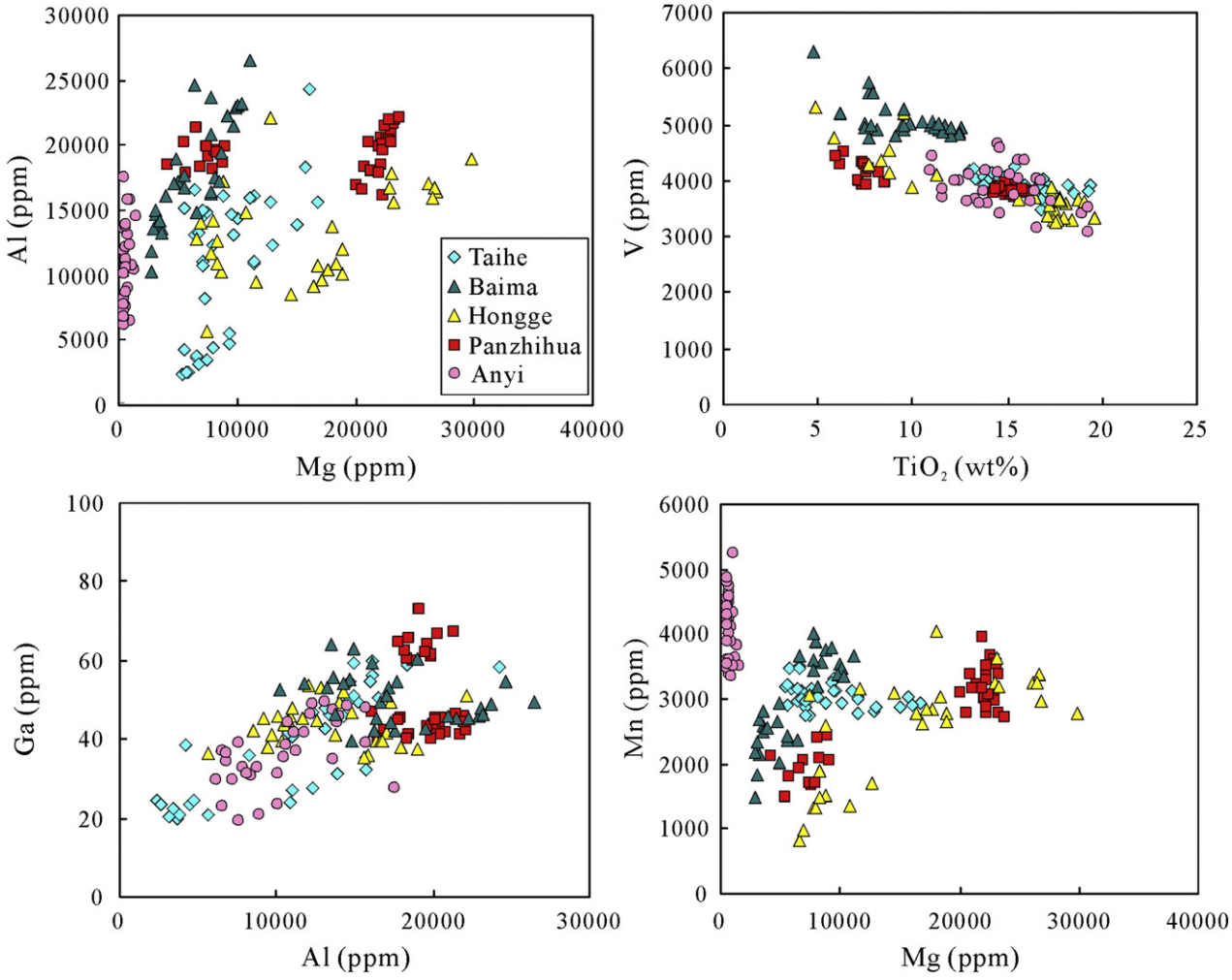

Fig. 7. Bi-elemental variation diagrams of Al vs. Mg (ppm), V (ppm) vs. TiO_2 (wt.%), Ga vs. Al (ppm) and Mn vs. Mg (ppm) of magnetite from Fe–Ti oxide ores of the Taihe, Baima, Hongge, Panzhihua and Anyi deposits in ELIP.

6.1.1. Effect of oxidation–exsolution

Ilmenite, spinel and magnetite intergrowths are common in volcanic and plutonic rocks (von Gruenewaldt et al., 1985). They can form by oxidation of magnetite-ulvöspinel solid solutions at subsolidus temperatures. Oxidation–exsolution of magnetite commonly involves the removal of Ti, Al and Mg to form ilmenite and spinel, accompanied by local redistribution of Sc, Ti, Mn, Nb, Sn, Ta and W, which are more compatible in ilmenite than in magnetite (Buddington and Lindsley, 1964). Exsolution patterns and fabrics vary with increasing degrees of oxidation and diffusion, resulting in a systematic series of microtextures from a single-phase homogeneous ulvöspinel grain, through trellis or sandwich intergrowths of ilmenite lamellae to granules of ilmenite within or on the external borders of magnetite (Buddington and Lindsley, 1964). Microtextures of magnetite in the Fe–Ti–(V) oxide ore deposits of the ELIP (Figs. 3 and 4) indicate that they belong to oxidation–exsolution stage of trellis or sandwich intergrowths of ilmenite lamellae. This process can be expressed in the equation

$$6Fe_2TiO_4 + O_2 = 6FeTiO_3 + 2Fe_3O_4,$$

where extra oxygen may come from water and other fluids (Verhoogen, 1962). The influence of oxygen fugacity on magnetite composition is obvious. Toplis and Corgne (2002) have determined experimentally that magnetite becomes more enriched in TiO_2 and V_2O_3 with decreasing oxygen fugacities under the same magmatic conditions, whereas divalent cations such as Ca, Co, Ni, Mn and Mg have no systematic dependence on oxygen fugacity. Micro-exsolution of ilmenite and spinel, on the other hand, remarkably affects the analyses of magnetite acquired using EMP, which display variable amounts (>two orders of magnitude) of TiO_2, MgO and Al_2O_3 even in the same type of ores (Wang and Zhou, 2013; Zhou et al., 2013). However, during LA-ICP-MS analyses of magmatic magnetite, both the magnetite host and its minute and commonly homogeneous exsolution products are ablated so that the analyses represent magnetite compositions before lamellae exsolution. This can be demonstrated by comparing the analytical results of EMP and LA-ICP-MS (Fig. 5). Magnetite compositions of the Panzhihua, Hongge, Baima and Anyi intrusions obtained by EMP, project on a large field in the Al_2O_3 vs. TiO_2 and V_2O_3 vs. MgO diagrams (Fig. 5, Zhou et al., 2013). The variable contents of TiO_2 result from ilmenite ($FeTiO_3$) exsolution whereas the large variations of Al_2O_3 and MgO are due to spinel ($MgAl_2O_4$) exsolution. However, data obtained by LA-ICP-MS plot within a much smaller field and are most likely to be centered in the large field outlined by EMP data, indicating homogenization of those exsolution lamellae by a large spot size. Thus, LA-ICP-MS analyses obtained by large spot size could represent the composition of the original magnetite.

6.1.2. Magma composition and coexisting minerals

Trace elements of magnetite may bear important information about the compositions of magmas from which it was crystallized (Dare et al., 2012; Dupuis and Beaudoin, 2011; Frost and Lindsley, 1991; Gao et al.,

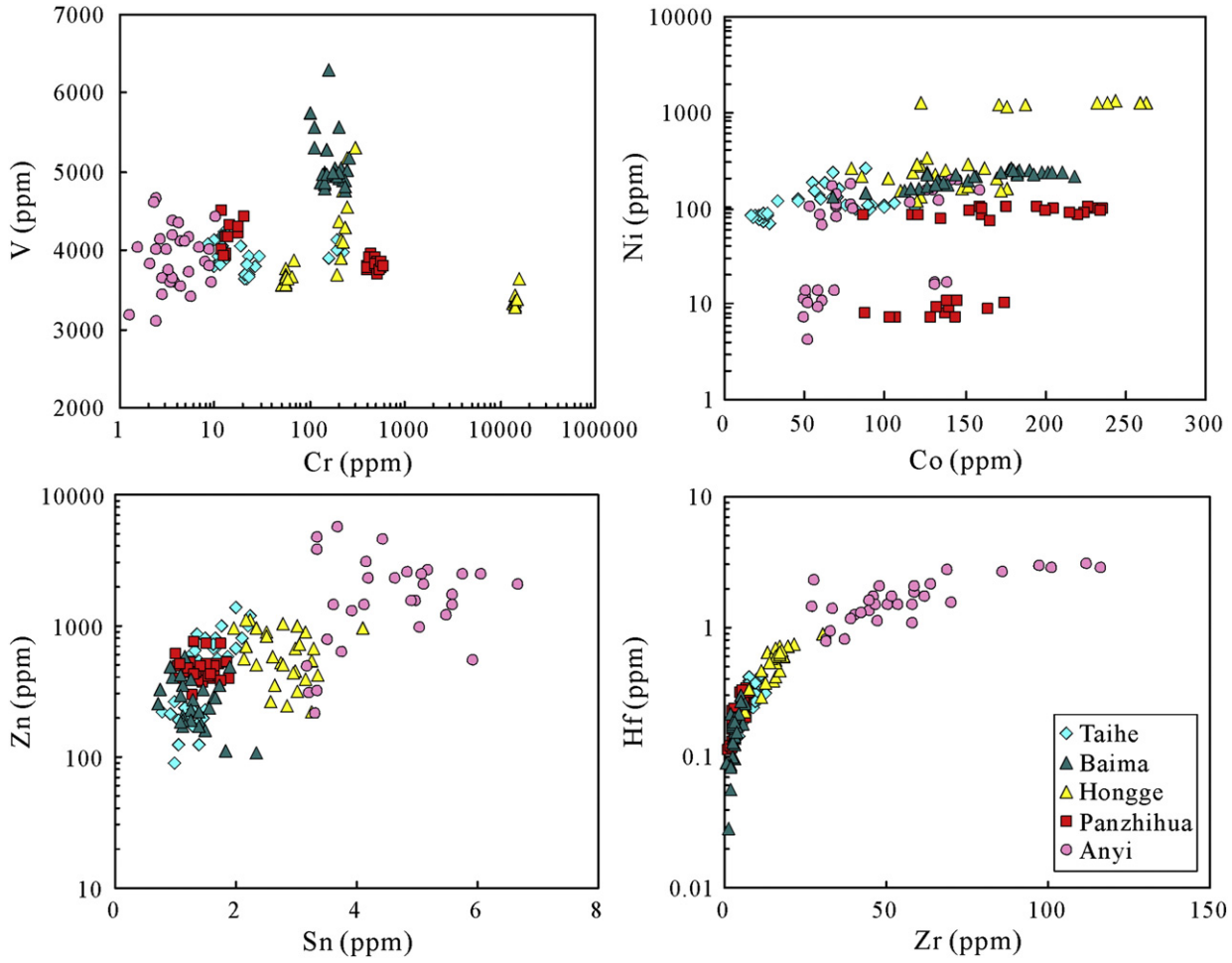

Fig. 8. Bi-elemental variation diagrams of V vs. Cr (ppm), Ni vs. Co (ppm), Zn vs. Sn (ppm) and Hf vs. Zr (ppm) of magnetite from Fe–Ti oxide ores of the Taihe, Baima, Hongge, Panzhihua and Anyi deposits in ELIP.

2013; Huang et al., 2013; McCarthy and Cawthorn, 1983; Nadoll et al., 2014). The control of magma composition on magmatic magnetite, on the other hand, is directly correlated to the mineral that is co-crystallizing from the same melt.

Fe–Ti–(V) oxide-bearing mafic–ultramafic intrusions in the ELIP are suggested to be related to high-Ti picritic magmas derived from the Emeishan mantle plume (Wang et al., 2014; Zhou et al., 2008, 2013). The parental magmas for the mafic–ultramafic intrusions in the ELIP may have evolved from the high-Ti picritic magmas. Thus, magma compositions of these deposits can possibly affect the concentrations of the elements partitioned into magnetite. The high Ta and Nb, and low Mg and Cr contents of magnetite from the Anyi deposit may indicate that it crystallized from more evolved magmas compared to the other deposits. The Hongge deposit, in contrast, may have formed from less evolved magmas because of its high Cr and low Ta and Nb contents (Fig. 6).

The origin of magnetite in layered intrusions is highly debated. There are mainly two schools of thoughts: 1) crystallization of magnetite from Fe–Ti–(P) rich immiscible liquids (Jakobsen et al., 2005, 2011; Liu et al., 2014a; Reynolds, 1985; Ripley et al., 1998; VanTongeren and Mathez, 2012; Wang and Zhou, 2013; Zhou et al., 2013) and 2) early crystallization of magnetite from basaltic magmas (Pang et al., 2008b, 2009; Shellnutt and Pang, 2012; Tegner et al., 2006). The former scenario commonly involves the separation of Fe-rich and Si-rich liquids, resulting in enrichment of P (by a factor of 10), rare earth elements (REEs), Ta, Ca, Cr, Ti, Mn, Zr, Mg, Sr and Ba (by a factor of 1.5) in Fe-rich liquids (Watson, 1976). In this case, olivine, clinopyroxene and plagioclase crystallize from the Si-rich liquids whereas magnetite, ilmenite and apatite crystallize from the Fe-rich liquids (Liu et al., 2014a). Saturation of apatite and ilmenite will dramatically reduce the concentrations of REEs, Sr, U and Th, which are preferentially partitioned into apatite (Watson and Capobianco, 1981; Watson and Green, 1981) and those of Mg, Sc, Ti, Mn, Nb, Sn, Ta and W, which are more enriched in ilmenite compared with those in magnetite (Dare et al., 2012). In the second scenario, magnetite usually crystallizes late after olivine, pyroxenes and plagioclase. Most trace elements, except Ni and Li which have partition coefficients of ~1, are incompatible in olivine (Dunn and Sen, 1994; Hart and Dunn, 1993; Johnson, 1998). Crystallization of clinopyroxene and plagioclase, on the other hand, would deplete Sc, Sr and Ba in residual magmas (Dunn and Sen, 1994; Nielsen et al., 1992). Considering that Li, Sr and Ba are all incompatible elements in magnetite (Dare et al., 2012; Toplis and Corgne, 2002), crystallization of olivine, pyroxenes and plagioclase barely has any significant effect on the trace element partitioning of magnetite. However, early crystallization of chromite or Cr-rich magnetite would deplete Cr concentrations in the residual magmas and in magnetite crystallized later. Magnetite from the Hongge intrusion falls into two groups in terms of Cr contents: >10,000 ppm and <1000 ppm with a big gap in between. This is consistent with the data reported by Wang and Zhou (2013), which includes a systematic set of samples. This compositional gap of the highly compatible element Cr ($D_{Cr}^{magnetite/melt}$ = 100–600; McCarthy et al., 1985) in magnetite is discordant with the scenario of fractional crystallization of magnetite from the ferrobasaltic magmas, whose Cr contents are expected to decrease dramatically and continuously. The low but relatively homogeneous

Table 2
EMP results of ilmenite from magmatic Fe–Ti oxide ore deposits in the ELIP.

Deposit	Taihe									Panzhihua						Hongge					
Sample	TH11-10			TH11-7			TH11-1			PZ2			PZ1			HG11-35			HG11-27		
Point no.	1	2	3	1	2	3	1	2	3	1	2	3	1	2	3	1	2	3	1	2	3
MgO	4.85	5.33	7.85	2.71	4.37	4.22	1.67	1.95	4.48	7.67	7.65	7.86	3.77	3.62	3.68	3.95	4.45	5.07	9.58	9.65	9.24
MnO	0.64	0.69	0.49	0.98	0.71	0.71	1.21	1.08	0.74	0.51	0.48	0.48	0.60	0.70	0.67	0.71	0.69	0.68	0.41	0.40	0.37
TiO_2	54.4	54.7	55.1	53.7	51.2	53.6	52.4	52.8	52.9	55.2	54.7	54.4	52.6	51.2	51.3	53.0	53.0	52.7	55.2	56.0	56.3
Al_2O_3	0.02	0.02	0.04	0.01	0.11	0.01	0.03	0.03	0.01	0.01	0.06	0.03	0.03	0.11	0.04	0.02	0.02	0.02	0.03	0.07	0.02
FeO	39.7	38.4	36.0	42.4	42.5	40.6	43.4	42.8	40.9	36.4	36.4	35.9	42.3	43.5	43.5	41.3	40.6	40.5	34.1	33.4	33.3
V_2O_3	0.45	0.45	0.46	0.41	0.48	0.43	0.50	0.46	0.49	0.43	0.53	0.50	0.47	0.50	0.53	0.44	0.47	0.49	0.48	0.45	0.46
Total	100	99.5	99.9	100	99.4	99.6	99.2	99.1	99.5	100	99.8	99.2	99.8	99.6	99.7	99.4	99.3	99.5	99.8	100	99.7

Deposit	Hongge			Anyi								Baima										
Sample	HG11-21			AY11-80			AY11-40			AY11-37		BM12-125			BM12-127			BM12-126		BM12-124		
Point no.	1	2	3	1	2	3	1	2	3	1	2	1	2	3	1	2	3	1	2	1	2	3
MgO	9.37	9.34	9.81	0.06	0.07	0.05	0.04	0.05	0.05	0.08	0.08	2.14	1.60	1.73	2.55	2.41	2.61	4.05	4.03	3.84	3.80	3.65
MnO	0.46	0.44	0.43	1.62	1.67	1.61	1.52	1.51	1.47	1.40	1.43	0.90	1.07	1.17	0.71	0.75	0.71	0.80	0.76	0.79	0.79	0.74
TiO_2	55.2	56.1	54.3	51.0	52.0	52.0	51.0	51.6	50.3	47.9	50.2	52.6	51.9	51.3	51.9	52.3	51.8	53.0	53.1	52.3	52.1	52.5
Al_2O_3	0.17	0.02	2.78	0.03	0.04	0.08	–	0.03	0.02	0.02	0.17	0.04	0.02	0.03	0.02	0.01	0.02	0.03	0.02	0.18	0.03	0.04
FeO	34.8	33.3	32.7	46.3	45.9	45.9	46.2	46.0	47.0	48.6	46.6	43.6	44.3	44.4	43.6	44.1	44.3	41.0	41.7	41.9	41.8	42.0
V_2O_3	0.47	0.55	0.46	0.53	0.46	0.54	0.39	0.52	0.55	0.07	–	0.46	0.43	0.51	0.52	0.47	0.49	0.39	0.47	0.50	0.50	0.47
Total	100	99.8	100	99.5	100	100	99.2	99.7	99.4	98.3	98.7	99.8	99.3	99.2	99.3	100	99.9	99.2	100	99.5	99.1	99.4

compatible trace elements (e.g. Cr and V) of magnetite also indicate contemporaneous crystallization of magnetite from similar melts. Thus, the characteristics of the compatible trace elements in magnetite from the Fe–Ti oxide ores of the ELIP favor its crystallization from homogeneous Fe-rich melts, consistent with a recent model proposed by Liu et al. (2014a) based on evidence of multiphase solid inclusions.

6.2. Oxygen fugacities of the Fe–Ti–(V) oxide deposits in the Panxi region

Compositions of magnetite and ilmenite pairs can be used to calculate temperature and oxygen fugacity (fO_2) conditions at which these minerals last equilibrated (Andersen et al., 1993; Buddington and Lindsley, 1964). During cooling of the oxide minerals in the ores, inter-oxide re-equilibration (Frost and Lindsley, 1992; Frost et al., 1988) represented by the exchange of Fe and Ti between magnetite and ilmenite, following the coupled substitution of $Fe^{2+} + Ti^{4+} = 2Fe^{3+}$, expressed in the following equilibrium

$$Fe_2TiO_4(\text{in magnetite}) + Fe_2O_3(\text{in ilmenite}) = FeTiO_3(\text{in ilmenite}) + Fe_3O_4(\text{in magnetite}).$$

This reaction proceeds to the right with decreasing temperatures, causing magnetite and ilmenite to approach their end-member compositions of Fe_3O_4 and $FeTiO_3$, respectively.

We have conducted calculations on magnetite–ilmenite mineral pairs from the main oxide ore zone of the Taihe, Baima, Hongge, Panzhihua and Anyi intrusions using the QUILF program provided by Andersen et al. (1993). The results of fO_2 are reported as log units relative to the fayalite–magnetite–quartz buffer (FMQ). The calculated temperature and fO_2 range from 450 to 560 °C and ΔFMQ −3.1 to −4.6 for Taihe oxide ores, from 460 to 610 °C and ΔFMQ −1.0 to −4.0 for Panzhihua oxide ores, from 380 to 540 °C and ΔFMQ −2.9 to −5.2 for Hongge oxide ores, from 530 to 570 °C and ΔFMQ −2.1 to −3.1 for Baima oxide ores, and from 520 to 700 °C and ΔFMQ −1.1 to −3.7 for Anyi oxide ores (Fig. 10). All the data follow trends of decreasing fO_2 with decreasing temperature that lie sub-parallel to and within the ulvöspinel isopleths of U-20 and U-60.

Therefore, the end of subsolidus equilibration for magnetite and ilmenite of Panzhihua Fe–Ti oxide ores occurred at higher fO_2, followed by that of the Baima Fe–Ti oxide ores. Iron–Ti oxide ores of the Anyi, Taihe and Hongge deposits, on the other hand, formed at relatively low fO_2 conditions. We thus propose that the occurrence of massive and/or net-textured Fe–Ti oxide ores at the bottom of the Panzhihua and Baima intrusions were due to high oxygen fugacities of the parental magmas. The parental magmas of the Anyi, Taihe and Hongge intrusions, however, had relatively low oxygen fugacity, and thus crystallized net-textured and/or disseminated Fe–Ti oxide ores after a lengthy period of silicate fractionation. This suggests that the oxygen fugacity of the parental magma may have significant control on the amount and crystallization time of the Fe–Ti oxides.

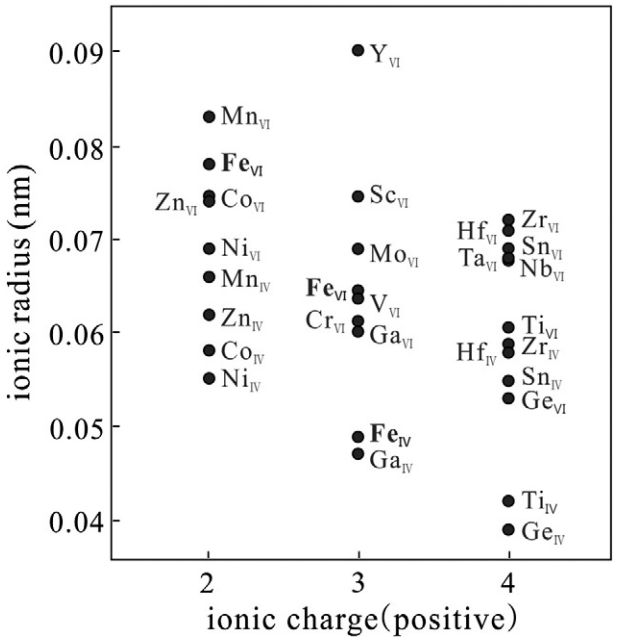

Fig. 9. Ionic radius vs. ionic charge diagram for common cations that can substitute for Fe^{3+} in the tetrahedral (IV) sites and Fe^{2+} or Fe^{3+} in the octahedral (VI) sites. Coupled substitution is required for the incorporation of 4+ cations such as Ti^{4+} to maintain charge balance.

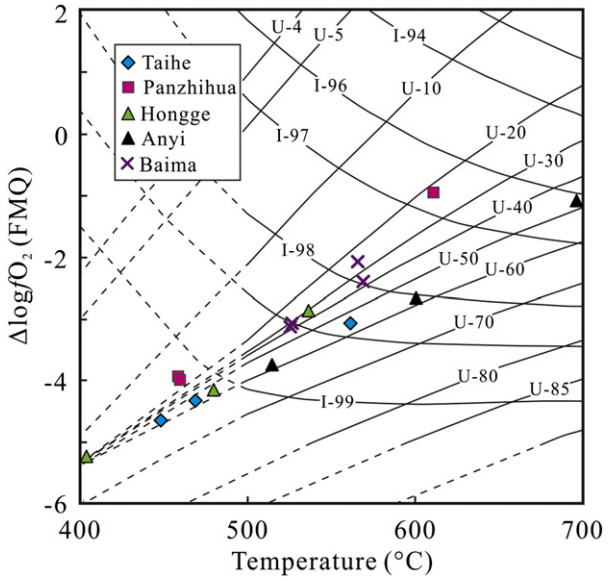

Fig. 10. ΔlogfO_2-temperature diagram constructed from compositions of coexisting magnetite and ilmenite pairs of the Taihe, Panzhihua, Hongge, Anyi and Baima Fe–Ti oxide ores. The ilmenite and ulvöspinel isopleths are after Frost et al. (1988). Dashed lines from temperatures of 400 to 500 °C or ΔlogfO_2 values between −5 and −6 are extrapolated lines represent possible temperature and oxygen fugacity conditions.

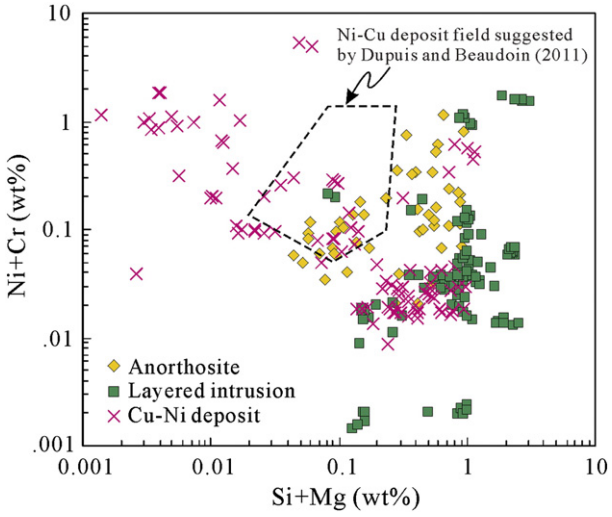

Fig. 11. Ni + Cr vs. Si + Mg discriminant diagram showing that compositions of magnetite from the Ni–Cu sulfide ores of Sudbury, Canada and the Huangshandong intrusion, NW China fall beyond the Ni–Cu deposit field (dashed lines) suggested by Dupuis and Beaudoin (2011). Magnetite from Damiao anorthosites and layered intrusions in ELIP can also plot within that Ni–Cu deposit field.

6.3. Magnetite as a provenance discriminator of different magmatic ore deposits

Discriminant diagrams are thought to be powerful in the identification of the provenance of refractory minerals, including zircon, rutile, spinel and magnetite (Barnes and Roeder, 2001; Basu and Molinaroli, 1991; Belousova et al., 2002; Dare et al., 2012; Grigsby, 1990; Hoskin and Ireland, 2000; Meinhold et al., 2008). These diagrams have been further applied to mineral deposits and help with identifying ore-deposition environments, ore deposit types and ore genesis (Carranza et al., 2012; Dupuis and Beaudoin, 2011; Nadoll et al., 2014; Pearce and Gale, 1977). The Ni–Cr–Si–Mg composition of magnetite, for example, has been used to distinguish a wide range of magmatic and hydrothermal mineral deposit types including iron oxide–copper–gold (IOCG), Kiruna apatite–magnetite, banded iron formation (BIF), porphyry Cu, Fe–Cu skarn, magmatic Fe–Ti–V–Cr or Ni–Cu–PGE, Cu–Zn–Pb volcanogenic massive sulfide (VMS) and Archean Au–Cu porphyry deposits (Dupuis and Beaudoin, 2011). However, the Ni + Cr vs. Si + Mg diagram has limitations in separating Cu–Ni sulfide deposits from Fe–Ti–(V) oxide deposits hosted in layered intrusions or anorthosites (Fig. 11). For example, the newly published magnetite data of Cu–Ni sulfide deposits from Sudbury, Canada (Dare et al., 2012) and Huangshandong intrusion, NW China (Gao et al., 2013) plot outside the designated Cu–Ni sulfide deposit field outlined by Dupuis and Beaudoin (2011) and magnetite from Fe–Ti oxide ores of Damiao anorthosites and layered intrusions of the ELIP plots within the field of Cu–Ni deposits. Thus this diagram alone is insufficient to distinguish Cu–Ni deposits and Fe–Ti–(V) oxide deposits.

The TiO_2–Al_2O_3–(MgO + MnO) triangular plot shows the relative proportions of the four most abundant trace elements in magmatic magnetite (Fig. 12, Appendix B and C). Magnetite from Fe–Ti oxide ores in ELIP layered intrusions has relatively uniform compositions of TiO_2, Al_2O_3 and MgO + MnO. It is more enriched in TiO_2 compared with Al_2O_3 and MgO + MnO. Magnetite from Cu–Ni sulfide deposits has the most varied TiO_2, Al_2O_3 and MgO + MnO contents. It is generally more enriched in MgO + MnO compared with that from layered intrusions and anorthosites (Fig. 12). One group of dots projects remarkably at the MgO + MnO end, indicating the dominance of MgO + MnO over TiO_2 and Al_2O_3. Magnetite from Fe–Ti oxide ores hosted in Damiao anorthosites also has large variations of TiO_2, Al_2O_3 and MgO + MnO compositions. It has the most (MgO + MnO)-depleted and Al_2O_3-enriched components. Similarly, multi-element variation diagrams of magnetite from Damiao anorthosites, Fe–Ti–(V) oxide ore deposit in the ELIP and Cu–Ni sulfide deposits in Sudbury and Huangshandong display different distribution patterns (Fig. 13). These differences in trace element contents are probably controlled by the parental magmas from which they were crystallized. Magmas to form Fe–Ti–(V) oxide deposits are generally high-Ti basalts and thus crystallize magnetite with high Ti, whereas magmas to form anorthosites would be enriched in Al but possibly depleted in Ti. Magmatic Cu–Ni sulfide deposits are generally formed from high-Mg magmas so that magnetite from these deposits would show an enrichment of Mg. Therefore, the (MgO + MnO)-enriched, TiO_2 and Al_2O_3-depleted magnetite can be characteristic of

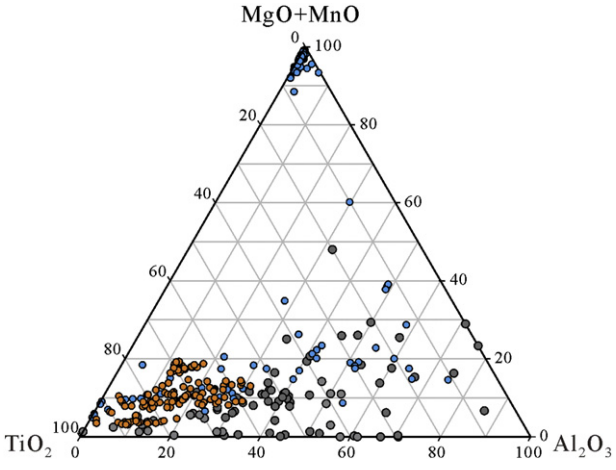

Fig. 12. Triangular diagram of TiO_2–Al_2O_3–(MgO + MnO) showing their relative proportions in magnetite from layered intrusions of the ELIP (orange circle), Cu–Ni sulfide deposit of Sudbury and Huangshandong (blue circle) and Damiao anorthosites (gray circle).

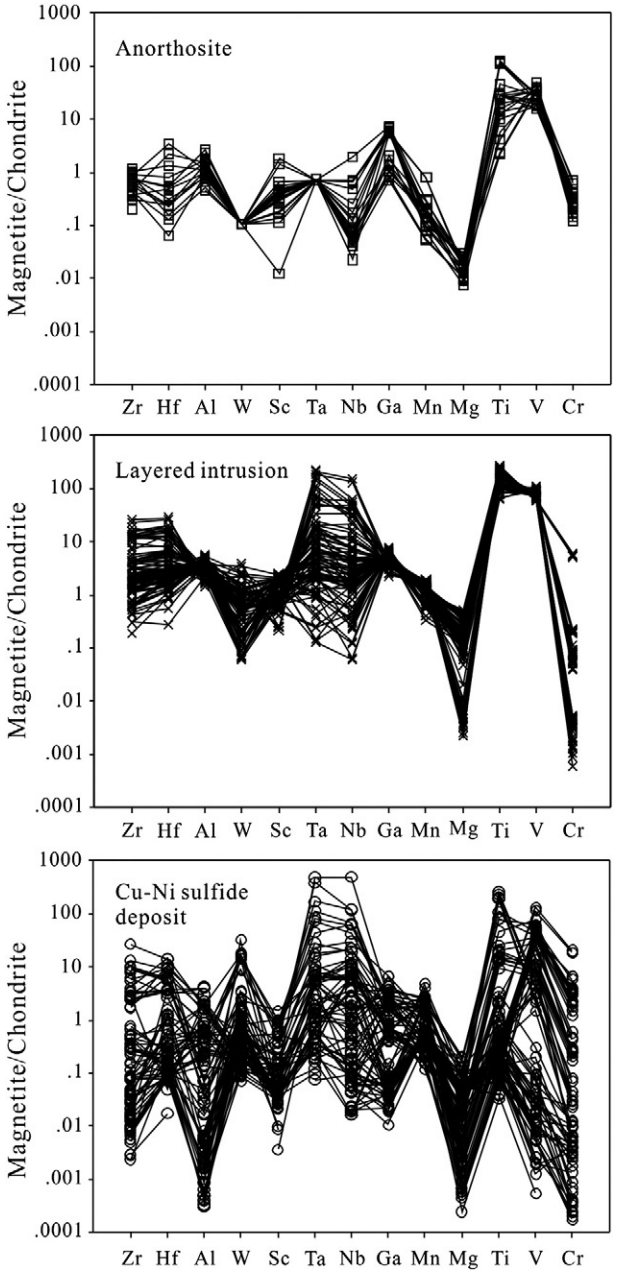

Fig. 13. Chondrite-normalized multi-element variation patterns for lithophile elements of magnetites from Fe–Ti–(P) oxide ores in the Damiao anorthosite massif, northern North China Craton, Fe–Ti oxide ores in layered intrusions of the ELIP and magmatic Cu–Ni sulfide ores in Sudbury, Canada and Huangchangdong, northwest China.
Values of CI carbonaceous chondrites are from McDonough and Sun (1995).

magnetites from Cu–Ni sulfide deposits and (MgO + MnO)-depleted, Al_2O_3-enriched magnetite of those from massif anorthosites.

Trace elements in magnetite could be more useful than the major elements for discriminating deposit types. For example, in the plots of Ge vs. Ga + Co, magnetites from mafic–ultramafic intrusions of the ELIP are separated from those from Fe–Ti oxide ores hosted in the Damiao anorthosite massif (Fig. 14). Compositions of magnetites from Cu–Ni deposits are relatively scattered (Fig. 14). Magnetites from oxide ores of anorthosites have higher Ge and lower Ga + Co contents than those from layered intrusions. Magnetites from Cu–Ni deposits have the lowest Ga + Co contents. We thus propose that the Ge vs. Ga + Co diagram can serve as a discrimination diagram for magnetites from layered intrusions and from massif anorthosites. Further case studies will be required to test if such a diagram is broadly applicable.

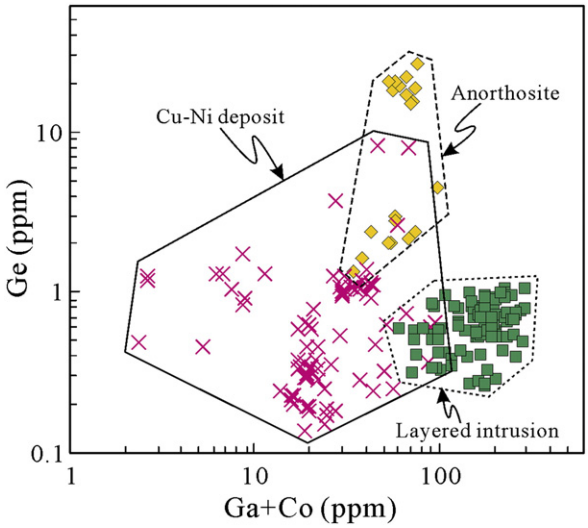

Fig. 14. Plots of Ge vs. Ga + Co for discriminating magnetites from Fe–Ti–(P) oxide ore-hosted anorthosite and Fe–Ti–(V) oxide-bearing layered intrusions. Magnetites from Cu–Ni sulfide deposits are more scattered and partially overlapped with other magnetites.

7. Conclusions

Spot analyses of LA-ICP-MS can yield original magnetite composition by ablating both magnetite and its exsolution products and are thus powerful in analyzing high-temperature magmatic magnetite. Crystallography, magma composition, co-crystallizing mineral phases and oxygen fugacity are primary factors that control the trace element contents of magmatic magnetite. QUILF equilibrium calculation shows that the amount and crystallization time of Fe–Ti oxide ores may depend on the oxygen fugacity of the parental magma. Concentrations of highly incompatible elements such as Cr and V in magnetite of the Fe–Ti–(V) oxide ore deposits of the ELIP indicate its crystallization from Fe-rich liquids instead of fractional crystallization from ferrobasaltic magmas. Trace element variations of magnetites from Cu–Ni sulfide deposits, Fe–Ti–(V) oxide ore-bearing mafic–ultramafic intrusions and Fe–Ti–(P) oxide ore-bearing anorthosites are probably controlled by the parental magmas from which they were crystallized. Plots of Ge vs. Ga + Co can be used to discriminate these magnetites.

Supplementary data to this article can be found online at http://dx.doi.org/10.1016/j.oregeorev.2014.09.002.

Acknowledgment

We are grateful to Prof. Yuxiao Ma, Mr. Guanghua He and Mr. Hong Liu for the fieldwork arrangements in the Baima mine, and Engineer Shuguang Gui and Xiangshen Xia from the Baima mining company for helping with field work. We acknowledge Prof. Liang Qi for helping with LA-ICP-MS analyses, Dr. Benxun Su, Mr. Wen Winston Zhao and Mr. Changming Xing for their helpful discussions. Ms. Diane Chung is thanked for reading an earlier version of the manuscript. Dr. Gregory Shellnutt and an anonymous reviewer are appreciated for the constructive comments which improved the manuscript a lot. This study is supported by the Research Grant Council of Hong Kong (HKU707012P) and by the CAS/SAFEA International Partnership Program for Creative Research Teams—Intraplate Mineralization Research Team (KZZDEW-TZ-20).

References

Ali, J.R., Lo, C.-h, Thompson, G.M., Song, X., 2004. Emeishan basalt Ar–Ar overprint ages define several tectonic events that affected the western Yangtze platform in the Mesozoic and Cenozoic. J. Asian Earth Sci. 23, 163–178.
Ali, J.R., Thompson, G.M., Zhou, M.-F., Song, X., 2005. Emeishan large igneous province, SW China. Lithos 79, 475–489.

Andersen, D.J., Lindsley, D.H., Davidson, P.M., 1993. QUILF: a Pascal program to assess equilibria among Fe–Mg–Mn–Ti oxides, pyroxenes, olivine, and quartz. Comput. Geosci. 19, 1333–1350.
Bai, Z.-J., Zhong, H., Naldrett, A.J., Zhu, W.-G., Xu, G.-W., 2012. Whole-rock and mineral composition constraints on the genesis of the giant Hongge Fe–Ti–V oxide deposit in the Emeishan large igneous province, southwest China. Econ. Geol. 107, 507–524.
Barnes, S.J., Roeder, P.L., 2001. The range of spinel compositions in terrestrial mafic and ultramafic rocks. J. Petrol. 42, 2279–2302.
Basu, A., Molinaroli, E., 1991. Reliability and application of detrital opaque Fe–Ti oxide minerals in provenance determination. Geol. Soc. Lond. Spec. Publ. 57, 55–65.
Belousova, E., Griffin, W.L., O'Reilly, S.Y., Fisher, N., 2002. Igneous zircon: trace element composition as an indicator of source rock type. Contrib. Mineral. Petrol. 143, 602–622.
Bookstrom, A.A., 1995. Magmatic features of iron ores of the Kiruna type in Chile and Sweden; ore textures and magnetite geochemistry; discussion. Econ. Geol. 90, 469–473.
Bragg, W., 1915. The structure of magnetite and the spinels. Nature 95, 561.
Buddington, A.F., Lindsley, D.H., 1964. Iron–titanium oxide minerals and synthetic equivalents. J. Petrol. 5, 310–357.
Burchfiel, B., Zhiliang, C., Yupinc, L., Royden, L., 1995. Tectonics of the Longmen Shan and adjacent regions, central China. Int. Geol. Rev. 37, 661–735.
Carmichael, I.S.E., 1966. The iron–titanium oxides of salic volcanic rocks and their associated ferromagnesian silicates. Contrib. Mineral. Petrol. 14, 36–64.
Carranza, E.J.M., Rondeau, B., Cenki-Tok, B., Fritsch, E., Mazzero, F., Gauthier, J., Bodeur, Y., Bekele, E., Gaillou, E., Ayalew, D., 2012. Geochemical characteristics of mineral deposits: implications for ore genesis. Geochem. Explor. Environ. Anal. 12, 89.
Chung, S.-L., Jahn, B.-m, 1995. Plume–lithosphere interaction in generation of the Emeishan flood basalts at the Permian–Triassic boundary. Geology 23, 889–892.
Chung, D., Zhou, M.-F., Gao, J.F., Chen, T.W., 2015. In-situ LA-ICP-MS trace elemental analyses of magnetite: the Paleoproterozoic Sokoman Iron Formation in the Labrador Trough, Canada. Ore Geol. Rev. 65, 917–928.
Cornell, R.M., Schwertmann, U., 2003. The iron oxides: structure, properties, reactions, occurrences and uses. www.Wiley.com.
Dare, S.A.S., Barnes, S.-J., Beaudoin, G., 2012. Variation in trace element content of magnetite crystallized from a fractionating sulfide liquid, Sudbury, Canada: implications for provenance discrimination. Geochim. Cosmochim. Acta 88, 27–50.
Duncan, A.R., Taylor, S.R., 1968. Trace element analyses of magnetites from andesitic and dacitic lavas from Bay of Plenty, New Zealand. Contrib. Mineral. Petrol. 20, 30–33.
Dunn, T., Sen, C., 1994. Mineral/matrix partition coefficients for orthopyroxene, plagioclase, and olivine in basaltic to andesitic systems: a combined analytical and experimental study. Geochem. Explor. Environ. Anal. 58, 717–733.
Dupuis, C., Beaudoin, G., 2011. Discriminant diagrams for iron oxide trace element fingerprinting of mineral deposit types. Miner. Deposita 46, 319–335.
Dymek, R.F., Klein, C., 1988. Chemistry, petrology and origin of banded iron-formation lithologies from the 3800 Ma Isua supracrustal belt, West Greenland. Precambrian Res. 39, 247–302.
Frost, B., Lindsley, D.H., 1991. Occurrence of iron–titanium oxides in igneous rocks. Rev. Mineral. Geochem. 25, 433–468.
Frost, B.R., Lindsley, D.H., 1992. Equilibria among Fe–Ti oxides, pyroxenes, olivine, and quartz: part II, application. Am. Mineral. 77, 1004–1020.
Frost, B.R., Lindsley, D.H., Andersen, D.J., 1988. Fe–Ti oxide–silicate equilibria: assemblages with fayalitic olivine. Am. Mineral. 73, 727–740.
Ganino, C., Arndt, N.T., Zhou, M.F., Gaillard, F., Chauvel, C., 2008. Interaction of magma with sedimentary wall rock and magnetite ore genesis in the Panzhihua mafic intrusion, SW China. Miner. Deposita 43, 677–694.
Gao, J.-F., Zhou, M.-F., Lightfoot, P.C., Wang, C.Y., Qi, L., Sun, M., 2013. Sulfide saturation and magma emplacement in the formation of the Permian Huangshandong Ni–Cu sulfide deposit, Xinjiang, northwestern China. Econ. Geol. 108, 1833–1848.
Ghiorso, M., Sack, O., 1991. Fe–Ti oxide geothermometry: thermodynamic formulation and the estimation of intensive variables in silicic magmas. Contrib. Mineral. Petrol. 108, 485–510.
Goldschmidt, V.M., 1937. The principles of distribution of chemical elements in minerals and rocks. The seventh Hugo Müller Lecture, delivered before the Chemical Society on March 17th, 1937. J. Chem. Soc. 655–673.
Grigsby, J.D., 1990. Detrital magnetite as a provenance indicator. J. Sediment. Res. 60, 940–951.
Groves, D.I., Bierlein, F.P., Meinert, L.D., Hitzman, M.W., 2010. Iron oxide copper–gold (IOCG) deposits through Earth history: implications for origin, lithospheric setting, and distinction from other epigenetic iron oxide deposits. Econ. Geol. 105, 641–654.
Hart, S.R., Dunn, T., 1993. Experimental cpx/melt partitioning of 24 trace elements. Contrib. Mineral. Petrol. 113, 1–8.
He, B., Xu, Y.-G., Chung, S.-L., Xiao, L., Wang, Y., 2003. Sedimentary evidence for a rapid, kilometer-scale crustal doming prior to the eruption of the Emeishan flood basalts. Earth Planet. Sci. Lett. 213, 391–405.
Hoskin, P.W., Ireland, T.R., 2000. Rare earth element chemistry of zircon and its use as a provenance indicator. Geology 28, 627–630.
Howarth, G.H., Prevec, S.A., Zhou, M.-F., 2013. Timing of Ti-magnetite crystallisation and silicate disequilibrium in the Panzhihua mafic layered intrusion: Implications for ore-forming processes. Lithos 170–171, 73–89.
Huang, X.-W., Zhou, M.-F., Qi, L., Gao, J.-F., Wang, Y.-W., 2013. Re–Os isotopic ages of pyrite and chemical composition of magnetite from the Cihai magmatic–hydrothermal Fe deposit, NW China. Miner. Deposita 48, 925–946.
Huang, X.-W., Gao, J.-F., Qi, L., Zhou, M.-F., 2015. In-situ LA-ICP-MS trace elemental analyses of magnetite and Re–Os dating of pyrite: the Tianhu hydrothermally remobilized sedimentary Fe deposit, NW China. Ore Geol. Rev. 65, 900–916.
Jakobsen, J.K., Veksler, I.V., Tegner, C., Brooks, C.K., 2005. Immiscible iron- and silica-rich melts in basalt petrogenesis documented in the Skaergaard intrusion. Geology 33, 885–888.
Jakobsen, J.K., Veksler, I.V., Tegner, C., Brooks, C.K., 2011. Crystallization of the Skaergaard intrusion from an emulsion of immiscible iron- and silica-rich liquids: evidence from melt inclusions in plagioclase. J. Petrol. 52, 345–373.
Johnson, K.T., 1998. Experimental determination of partition coefficients for rare earth and high-field-strength elements between clinopyroxene, garnet, and basaltic melt at high pressures. Contrib. Mineral. Petrol. 133, 60–68.
Jurek, K., Hulínský, V., 1980. The use and accuracy of the ZAF correction procedure for the microanalysis of glasses. Microchim. Acta 73, 183–198.
Klein, C., 2005. Some Precambrian banded iron-formations (BIFs) from around the world: their age, geologic setting, mineralogy, metamorphism, geochemistry, and origins. Am. Mineral. 90, 1473–1499.
Klemm, D.D., Henckel, J., Dehm, R.M., Von Gruenewaldt, G., 1985. The geochemistry of titanomagnetite in magnetite layers and their host rocks of the eastern Bushveld Complex. Econ. Geol. 80, 1075–1088.
Kolker, A., 1982. Mineralogy and geochemistry of Fe–Ti oxide and apatite (nelsonite) deposits and evaluation of the liquid immiscibility hypothesis. Econ. Geol. 77, 1146–1158.
Lindsley, D.H., 1991. Experimental studies of oxide minerals. Rev. Mineral. Geochem. 25, 69–106.
Lister, G.F., 1966. The composition and origin of selected iron–titanium deposits. Econ. Geol. 61, 275–310.
Liu, Y., Hu, Z., Gao, S., Günther, D., Xu, J., Gao, C., Chen, H., 2008. In situ analysis of major and trace elements of anhydrous minerals by LA-ICP-MS without applying an internal standard. Chem. Geol. 257, 34–43.
Liu, P.-P., Zhou, M.-F., Chen, W.T., Boone, M., Cnudde, V., 2014a. Using multiphase solid inclusions to constrain the origin of the Baima Fe–Ti–(V) oxide deposit, SW China. J. Petrol. 55, 951–976.
Liu, P.-P., Zhou, M.-F., Wang, C.Y., Xing, C.-M., Gao, J.-F., 2014b. Open magma chamber processes in the formation of the Permian Baima mafic–ultramafic layered intrusion, SW China. Lithos 184–187, 194–208.
Ma, Y., Ji, X.T., Li, J.C., Huang, M., Kan, Z.Z., 2003. Mineral Resources of the Panzhihua Region. Sichuan Science and Technology Press, Chengdu (275 pp.).
McCarthy, T.S., Cawthorn, R.G., 1983. The geochemistry of vanadiferous magnetite in the Bushveld complex: implications for crystallization mechanisms in layered complexes. Miner. Deposita 18, 505–518.
McCarthy, T.S., Cawthorn, R.G., Wright, C.J., McIver, J.R., 1985. Mineral layering in the Bushveld Complex; implications of Cr abundances in magnetite from closely spaced magnetitite and intervening silicate-rich layers. Econ. Geol. 80, 1062–1074.
McDonough, W.F., Sun, S.S., 1995. The composition of the Earth. Chem. Geol. 120, 223–253.
Meinhold, G., Anders, B., Kostopoulos, D., Reischmann, T., 2008. Rutile chemistry and thermometry as provenance indicator: an example from Chios Island, Greece. Sed. Geol. 203, 98–111.
Nadoll, P., Koenig, A.E., 2011. LA-ICP-MS of magnetite: methods and reference materials. J. Anal. At. Spectrom. 26, 1872–1877.
Nadoll, P., Mauk, J.L., Hayes, T.S., Koenig, A.E., Box, S.E., 2012. Geochemistry of magnetite from hydrothermal ore deposits and host rocks of the Mesoproterozoic Belt Supergroup, United States. Econ. Geol. 107, 1275–1292.
Nadoll, P., Angerer, T., Mauk, J.L., French, D., Walshe, J., 2014. The chemistry of hydrothermal magnetite: a review. Ore Geol. Rev. 61, 1–32.
Nielsen, R.L., Beard, J.S., 2000. Magnetite–melt HFSE partitioning. Chem. Geol. 164, 21–34.
Nielsen, R.L., Gallahan, W.E., Newberger, F., 1992. Experimentally determined mineral–melt partition coefficients for Sc, Y and REE for olivine, orthopyroxene, pigeonite, magnetite and ilmenite. Contrib. Mineral. Petrol. 110, 488–499.
Pang, K.N., Li, C.S., Zhou, M.F., Ripley, E.M., 2008a. Abundant Fe–Ti oxide inclusions in olivine from the Panzhihua and Hongge layered intrusions, SW China: evidence for early saturation of Fe–Ti oxides in ferrobasaltic magma. Contrib. Mineral. Petrol. 156, 307–321.
Pang, K.N., Zhou, M.F., Lindsley, D., Zhao, D., Malpas, J., 2008b. Origin of Fe–Ti oxide ores in mafic intrusions: evidence from the Panzhihua intrusion, SW China. J. Petrol. 49, 295–313.
Pang, K.N., Li, C.S., Zhou, M.F., Ripley, E.M., 2009. Mineral compositional constraints on petrogenesis and oxide ore genesis of the late Permian Panzhihua layered gabbroic intrusion, SW China. Lithos 110, 199–214.
Panxi Geological Team, 1987. Ore Formation and Geology of the Hongge Fe–Ti–V Oxide Deposit in Sichuan. Geological Publishing House, Beijing.
Pearce, J.A., Gale, G., 1977. Identification of ore-deposition environment from trace-element geochemistry of associated igneous host rocks. Geol. Soc. Lond. Spec. Publ. 7, 14–24.
Philpotts, A.R., 1967. Origin of certain iron–titanium oxide and apatite rocks. Econ. Geol. 62, 303–315.
Qi, L., Zhou, M.F., 2008. Platinum-group elemental and Sr–Nd–Os isotopic geochemistry of Permian Emeishan flood basalts in Guizhou Province, SW China. Chem. Geol. 248, 83–103.
Reynolds, I.M., 1985. The nature and origin of titaniferous magnetite-rich layers in the upper zone of the Bushveld Complex; a review and synthesis. Econ. Geol. 80, 1089–1108.
Ripley, E.M., Severson, M.J., Hauck, S.A., 1998. Evidence for sulfide and Fe–Ti–P-rich liquid immiscibility in the Duluth Complex, Minnesota. Econ. Geol. 93, 1052–1062.
Schock, H.H., 1979. Distribution of rare-earth and other trace elements in magnetites. Chem. Geol. 26, 119–133.
She, Y.-W., Yu, S.-Y., Song, X.-Y., Chen, L.-M., Zheng, W.-Q., Luan, Y., 2014. The formation of P-rich Fe–Ti oxide ore layers in the Taihe layered intrusion, SW China: implications for magma-plumbing system process. Ore Geol. Rev. 57, 539–559.

Shellnutt, J.G., 2014. The Emeishan large igneous province: a synthesis. Geosci. Front. 5, 369–394.
Shellnutt, J.G., Pang, K.-N., 2012. Petrogenetic implications of mineral chemical data for the Permian Baima igneous complex, SW China. Miner. Petrol. 106, 75–88.
Shellnutt, J.G., Zhou, M.-F., 2007. Permian peralkaline, peraluminous and metaluminous A-type granites in the Panxi district, SW China: their relationship to the Emeishan mantle plume. Chem. Geol. 243, 286–316.
Shellnutt, J.G., Zhou, M.-F., 2008. Permian, rifting related fayalite syenite in the Panxi region, SW China. Lithos 101, 54–73.
Shellnutt, J.G., Zhou, M.F., Yan, D.P., Wang, Y.B., 2008. Longevity of the Permian Emeishan mantle plume (SW China): 1 Ma, 8 Ma or 18 Ma? Geol. Mag. 145, 373–388.
Shellnutt, J.G., Zhou, M.-F., Zellmer, G.F., 2009. The role of Fe–Ti oxide crystallization in the formation of A-type granitoids with implications for the Daly gap: an example from the Permian Baima igneous complex, SW China. Chem. Geol. 259, 204–217.
Shellnutt, J.G., Wang, K.-L., Zellmer, G.F., Iizuka, Y., Jahn, B.-M., Pang, K.-N., Qi, L., Zhou, M.-F., 2011. Three Fe–Ti oxide ore-bearing gabbro–granitoid complexes in the Panxi region of the Permian Emeishan large igneous province, SW China. Am. J. Sci. 311, 773–812.
Shellnutt, J.G., Denyszyn, S.W., Mundil, R., 2012. Precise age determination of mafic and felsic intrusive rocks from the Permian Emeishan large igneous province (SW China). Gondwana Res. 22, 118–126.
Song, X.Y., Zhou, M.F., Hou, Z.Q., Cao, Z.M., Wang, Y.L., Li, Y.G., 2001. Geochemical constraints on the mantle source of the upper permian Emeishan continental flood basalts, southwestern China. Int. Geol. Rev. 43, 213–225.
Song, X.-Y., Qi, H.-W., Hu, R.-Z., Chen, L.-M., Yu, S.-Y., Zhang, J.-F., 2013. Formation of thick stratiform Fe–Ti oxide layers in layered intrusion and frequent replenishment of fractionated mafic magma: evidence from the Panzhihua intrusion, SW China. Geochem. Geophys. Geosyst. 14, 712–732.
Tegner, C., Cawthorn, R.G., Kruger, F.J., 2006. Cyclicity in the main and upper zones of the Bushveld complex, South Africa: crystallization from a zoned magma sheet. J. Petrol. 47, 2257–2279.
Thompson, G.M., Ali, J.R., Song, X.Y., Jolley, D.W., 2001. Emeishan Basalts, SW China: reappraisal of the formation's type area stratigraphy and a discussion of its significance as a large igneous province. J. Geol. Soc. 158, 593–599.
Toplis, M.J., Carroll, M.R., 1995. An experimental study of the influence of oxygen fugacity on Fe–Ti oxide stability, phase relations, and mineral–melt equilibria in ferro-basaltic systems. J. Petrol. 36, 1137–1170.
Toplis, M., Corgne, A., 2002. An experimental study of element partitioning between magnetite, clinopyroxene and iron-bearing silicate liquids with particular emphasis on vanadium. Contrib. Mineral. Petrol. 144, 22–37.
VanTongeren, J.A., Mathez, E.A., 2012. Large-scale liquid immiscibility at the top of the Bushveld Complex, South Africa. Geology 40, 491–494.
Verhoogen, J., 1962. Oxidation of iron–titanium oxides in igneous rocks. J. Geol. 70, 168–181.
von Gruenewaldt, G., Klemm, D.D., Henckel, J., Dehm, R.M., 1985. Exsolution features in titanomagnetites from massive magnetite layers and their host rocks of the upper zone, eastern Bushveld Complex. Econ. Geol. 80, 1049–1061.
Wager, L.R., Brown, G.M., 1968. Layered Igneous Rock. Oliver & Boyd, Edinburgh (588 pp.).
Wang, C.Y., Zhou, M.-F., 2013. New textural and mineralogical constraints on the origin of the Hongge Fe–Ti–V oxide deposit, SW China. Miner. Deposita 48, 787–798.
Wang, C.Y., Zhou, M.-F., Qi, L., 2007. Permian flood basalts and mafic intrusions in the Jinping (SW China)–Song Da (northern Vietnam) district: mantle sources, crustal contamination and sulfide segregation. Chem. Geol. 243, 317–343.
Wang, C.Y., Zhou, M.-F., Yang, S., Qi, L., Sun, Y., 2014. Geochemistry of the Abulangdang intrusion: cumulates of high-Ti picritic magmas in the Emeishan large igneous province, SW China. Chem. Geol. 378, 24–39.
Watson, E.B., 1976. Two-liquid partition coefficients: experimental data and geochemical implications. Contrib. Mineral. Petrol. 56, 119–134.
Watson, E.B., Capobianco, C.J., 1981. Phosphorus and the rare earth elements in felsic magmas: an assessment of the role of apatite. Geochim. Cosmochim. Acta 45, 2349–2358.
Watson, E.B., Green, T.H., 1981. Apatite/liquid partition coefficients for the rare earth elements and strontium. Earth Planet. Sci. Lett. 56, 405–421.
Wechsler, B.A., Lindsley, D.H., Prewitt, C.T., 1984. Crystal structure and cation distribution in titanomagnetites ($Fe_{3-x}Ti_xO_4$). Am. Mineral. 69, 754–770.
Xiao, L., Xu, Y.G., Chung, S.L., He, B., Mei, H.J., 2003. Chemostratigraphic correlation of Upper Permian lavas from Yunnan Province, China: extent of the Emeishan large igneous province. Int. Geol. Rev. 45, 754–766.
Xiao, L., Xu, Y.G., Mei, H.J., Zheng, Y.F., He, B., Pirajno, F., 2004. Distinct mantle sources of low-Ti and high-Ti basalts from the western Emeishan large igneous province, SW China: implications for plume–lithosphere interaction. Earth Planet. Sci. Lett. 228, 525–546.
Xu, Y., Mei, H., Xu, J., Huang, X., Wang, Y., Chung, S.-L., 2003. Origin of two differentiation trends in the Emeishan flood basalts. Chin. Sci. Bull. 48, 390–394.
Xu, Y.G., Huang, X.-L., Ma, J.-L., Wang, Y.-B., Iizuka, Y., Xu, J.-F., Wang, Q., Wu, X.-Y., 2004. Crust–mantle interaction during the tectono-thermal reactivation of the North China Craton: constraints from SHRIMP zircon U–Pb chronology and geochemistry of Mesozoic plutons from western Shandong. Contrib. Mineral. Petrol. 147, 750–767.
Yin, A., Harrison, T.M., 2000. Geologic evolution of the Himalayan–Tibetan orogen. Annu. Rev. Earth Planet. Sci. 28, 211–280.
Yu, S.-Y., Song, X.-Y., Chen, L.-M., Li, X.-B., 2014. Postdated melting of subcontinental lithospheric mantle by the Emeishan mantle plume: evidence from the Anyi intrusion, Yunnan, SW China. Ore Geol. Rev. 57, 560–573.
Zhang, X.-Q., Song, X.-Y., Chen, L.-M., Xie, W., Yu, S.-Y., Zheng, W.-Q., Deng, Y.-F., Zhang, J.-F., Gui, S.-G., 2012. Fractional crystallization and the formation of thick Fe–Ti–V oxide layers in the Baima layered intrusion, SW China. Ore Geol. Rev. 49, 96–108.
Zhong, H., Zhou, X.H., Zhou, M.F., Sun, M., Liu, B.G., 2002. Platinum-group element geochemistry of the Hongge Fe–V–Ti deposit in the Pan–Xi area, southwestern China. Miner. Deposita 37, 226–239.
Zhou, M.-F., Malpas, J., Song, X.-Y., Robinson, P.T., Sun, M., Kennedy, A.K., Lesher, C.M., Keays, R.R., 2002a. A temporal link between the Emeishan large igneous province (SW China) and the end-Guadalupian mass extinction. Earth Planet. Sci. Lett. 196, 113–122.
Zhou, M.-F., Kennedy, A.K., Sun, M., Malpas, J., Lesher, C.M., 2002b. Neoproterozoic arc-related mafic intrusions along the northern margin of South China: implications for the accretion of Rodinia. J. Geol. 110, 611–618.
Zhou, M.-F., Yan, D.P., Kennedy, A.K., Li, Y.Q., Ding, J., 2002c. SHRIMP U–Pb zircon geochronological and geochemical evidence for Neoproterozoic arc-magmatism along the western margin of the Yangtze Block, South China. Earth Planet. Sci. Lett. 196, 51–67.
Zhou, M.-F., Robinson, P.T., Lesher, C.M., Keays, R.R., Zhang, C.J., Malpas, J., 2005. Geochemistry, petrogenesis and metallogenesis of the Panzhihua gabbroic layered intrusion and associated Fe–Ti–V oxide deposits, Sichuan province, SW China. J. Petrol. 46, 2253–2280.
Zhou, M.-F., Arndt, N.T., Malpas, J., Wang, C.Y., Kennedy, A.K., 2008. Two magma series and associated ore deposit types in the Permian Emeishan large igneous province, SW China. Lithos 103, 352–368.
Zhou, M.-F., Chen, W.T., Wang, C.Y., Prevec, S.A., Liu, Patricia P., Howarth, G.H., 2013. Two stages of immiscible liquid separation in the formation of Panzhihua-type Fe–Ti–V oxide deposits, SW China. Geosci. Front. 4, 481–502.